Spatial proteomics reveals lipid droplet reorganization in symbiotic *Paramecium bursaria* cells

Yan-Jun Chen[1], Md Mostafa Kamal[1*], Chuan-Chih Hsu[2], and Jun-Yi Leu[1*]

[1] Institute of Molecular Biology, Academia Sinica, Taipei, 11529, Taiwan

[2] Institute of Plant and Microbial Biology, Academia Sinica, Taipei, 11529, Taiwan

[*] Corresponding authors: mostafa.kamal42@gmail.com; jleu@as.edu.tw

Short title: **A spatial proteome of the *Paramecium bursaria***

Keywords: ciliate, endosymbiosis, protein subcellular localization, lipid droplet, proteomics

Abstract

Endosymbiosis is an important adaptive mechanism allowing organisms to exploit novel niches. The flexible relationship between the ciliate *Paramecium bursaria* and green algae represents a model system for studying early endosymbiosis evolution. However, the mechanisms underlying how *P. bursaria* cells maintain this endosymbiotic relationship remain unclear. Here, we use mass spectrometry-based proteomics to generate a spatial proteomic atlas of the host *P. bursaria* cells with and without endosymbionts. This atlas defines the protein composition of the endosymbiont-containing compartment (perialgal vacuole) and reveals pronounced remodeling of host lipid droplets upon symbiosis. Imaging analyses confirm that lipid droplets change in size, morphology, and positioning, accumulating near intracellular algae. Perturbing symbiotic cells with chemical inhibitors of lipid metabolism reduces endosymbiotic algal numbers, revealing a role for lipid droplets in the host-endosymbiont interaction. Our data provide a comprehensive resource for protein localization in *P. bursaria* cells and elucidate how those cells remodel an existing cellular compartment to maintain endosymbiosis.

Introduction

It is widely accepted that an ancient endosymbiotic event between an archaeal cell and an alpha-proteobacterium led to the formation of the eukaryotic cell with mitochondria (*1, 2*). The

32 establishment of endosymbiosis, a close relationship in which one organism (the endosymbiont)
33 lives within another (the host), is often driven by complementation between the endosymbiont
34 and host. Consequently, the interacting partners can explore new niches or resources inaccessible
35 to them when living alone (*3, 4*). Endosymbiosis has played a crucial role during the evolution of
36 eukaryotic cells. In addition to the formation of early eukaryotes, a second endosymbiosis event
37 generated the photosynthetic eukaryotic cell, leading to the evolution of algae and plants (*5, 6*).
38 Since those early events, endosymbiosis has occurred continuously and influenced the evolution
39 of various eukaryotic lineages (*7*). However, little is known about how endosymbiosis is
40 established initially and maintained.

41 The rapid increase in genomic data in recent years has facilitated the deciphering of
42 pathways potentially involved in host-endosymbiont interactions (*8, 9*). Nonetheless, only a few
43 of them have been validated experimentally. Ciliates have long been known to harbor various
44 endosymbionts, and it has been speculated that such associations enable ciliate populations to
45 dominate in certain marine and freshwater habitats (*10*). Among ciliates, *Paramecium bursaria* is
46 well known for its endosymbiotic relationship with green algae, which has fascinated
47 microbiologists for over a century (*11*). In the wild, most *P. bursaria* cells harbor several hundred
48 algal cells in their cytoplasm, and the endosymbionts can be stably transmitted to daughter cells
49 during cell division (*12*). However, symbiotic *P. bursaria* cells (symbiotic cells) can be
50 artificially induced to lose their algal cells and form aposymbiotic cells (aposymbiotic cells) (*13*).
51 When aposymbiotic *P. bursaria* cells are mixed with free-living *Chlorella* cells, they can quickly
52 reestablish endosymbiosis (*14*). Such flexibility allows scientists to observe and manipulate this
53 endosymbiotic relationship.

54 Although *Paramecium* species have long served as model systems for cell biology and
55 studies of endosymbiosis (*15*), only a small proportion of their protein-coding genes have been
56 functionally characterized (*16-18*). Even by integrating information on protein domains and
57 sequence homology, potential functions can only be assigned to approximately half of the 15000
58 protein-coding genes in the *P. bursaria* genome (*19*). Thus, a systematic approach is required to
59 understand the sheer complexity of these ciliate cells.

60 The emergence of novel subcellular compartments and the subsequent expansion of the
61 associated protein repertoire are key features of eukaryotic evolution. Ciliated protozoa represent
62 a lineage characterized by an abundance of unique subcellular compartments, and they also
63 possess some of the largest cells and gene families among all existing eukaryotes (*20*). In *P.*
64 *bursaria* cells, many subcellular compartments have been reported as involved in the process of

endosymbiosis, with the cytoplasmic space being extensively rearranged to facilitate hundreds of endosymbiotic algal cells (*21*).

Many biological processes are executed in specific organelles or subcellular compartments. Controlling protein abundance and localization enables a cell to regulate these processes accurately. Moreover, cells can remodel or reorganize their subcellular compartments to fine-tune their physiology in response to developmental or environmental cues. Dissecting protein abundance and localization under different conditions can facilitate our understanding of a protein's potential function and how cells adjust their physiology.

Recent advances in mass spectrometry-based proteomics have substantially improved our understanding of the protein landscape in various cell types (*22, 23*). To gain insights into how *P. bursaria* cells reorganize their subcellular structure to facilitate hundreds of endosymbiotic algae, we generated spatial proteomics maps of aposymbiotic and symbiotic *P. bursaria* cells. Our data reveal a significant increase in the proteins localizing to lipid droplets in symbiotic cells. Microscopic analysis further showed that the morphology and localization of lipid droplets change close to the endosymbiotic algae. Inhibiting lipid metabolism reduced the number of endosymbionts. Our study not only offers a comprehensive resource of protein localization and translocation data between two types of ciliate cells, but also reveals the involvement of lipid droplets in endosymbiosis.

Results

Whole-cell proteomic analysis of *Paramecium bursaria* using differential centrifugation

Although the cell biology of *P. bursaria* has been studied for decades, its genome was only decoded recently (*19, 24*). Nonetheless, a considerable proportion of its encoded proteins have unknown functions. We investigated the spatial distribution of the *P. bursaria* proteome, given that a protein's subcellular localization can provide information about its function (*25*). Moreover, many subcellular compartments are involved in the process of endosymbiosis (*26-28*). Thus, by comparing proteome maps of aposymbiotic and symbiotic cells, we anticipated gaining insights into how those subcellular compartments are reorganized to facilitate endosymbiosis.

We combined cell fractionation, shotgun proteomics, and machine-learning-based prediction to establish organellar protein localization (*29*). In brief, *P. bursaria* cells were lysed by nitrogen cavitation, and the subcellular compartments were separated by differential centrifugation. We collected 11 fractions, and the distinct protein patterns observed in the individual fractions indicated that our protocol successfully separated different subcellular compartments (fig. S1A and 1B). The collected fractions were subsequently analyzed by liquid

99 chromatography-mass spectrometry (LC-MS) in data-independent acquisition (DIA) mode, and
100 the resulting data were processed with Spectronaut for label-free quantitation (LFQ) analysis (Fig.
101 1A and data file S1A,B, see Methods for details). We analyzed three biological replicates for both
102 symbiotic and aposymbiotic cells. Protein identification was highly reproducible, with
103 approximately 95% of proteins shared across three replicates in both symbiotic and aposymbiotic
104 cells. Moreover, most proteins presented a low coefficient of variation (CV) between replicates,
105 indicative of high data quality (Fig. 1B and fig. S1C).
106 In addition to the fractionation samples, we also used mass spectrometry to analyze total
107 cell lysates, allowing us to compare the relative protein abundance of each protein between
108 symbiotic and aposymbiotic cells (data file S2). We detected 6,422 proteins in symbiotic cells and
109 6,216 proteins in aposymbiotic cells, with 6,135 overlapping between the two cell types. Since
110 our cell lysis protocol was optimized for *P. bursaria* host cells, the endosymbiotic algal cells were
111 not efficiently disrupted. Therefore, the algal proteome is not discussed in this study.
112
113 **Unsupervised clustering maps uncharacterized proteins to subcellular compartments**
114 To globally assess the separation efficiency of different cellular compartments, the fractionation
115 datasets were subjected to unsupervised clustering using hierarchical density-based spatial
116 clustering of applications with noise (HDBSCAN) (*30*). The algorithm evaluated the similarity of
117 protein abundance profiles across 33-plex fractions (from 33 fractions of three replicates) to
118 generate clusters. In total, 5389 proteins in symbiotic cells and 5533 proteins in aposymbiotic
119 cells showed distinct distribution patterns, generating 20 and 19 clusters, respectively (Fig. 2 and
120 data file S3A,B).
121 We utilized several well-conserved marker proteins of proteosomes, ribosomes, and ER, as
122 well as ciliate-specific trichocyst proteins, to examine whether these clusters represent meaningful
123 subcellular niches. These proteins are clearly grouped into clusters 6, 7, 8, and 1, indicating that
124 these subcellular compartments were well separated (fig. S2A). Gene ontology cellular
125 component (GOCC) enrichment analysis further supported that the clusters represent a diverse set
126 of relevant biological niches within the cell (Fig. 2 and data file S3C,D). Clusters 1-12 are highly
127 enriched with GOCC terms related to trychocyst, basal body, mitochondria, lytic vacuole,
128 proteasome, ribosome, ER, nucleus, and Golgi. In some cases, sub-compartment resolution was
129 observed (data file S3C,D). For example, proteins related to the mitochondrial envelope and
130 matrix (clusters 3 and 4 in Fig. 2), as well as those related to the nucleolus and nucleoplasm
131 (clusters 9 and 10 in Fig. 2), were separated into distinct clusters in both cell types. These data
132 indicate that our fractionation data can be used to generate a high-resolution spatial proteomic

133 map. On the other hand, the disruption of cellular compartments during fractionation may lead to
134 divergent distribution patterns among proteins from the same compartment.
135 Symbiotic cells form a specific membrane compartment, the perialgal vacuole (PV), to
136 accommodate endosymbiotic algae (*31, 32*). We investigated whether one of the HDBSCAN
137 clusters was formed by the proteins of PVs. Several criteria were applied in selecting the
138 candidate PV cluster. First, we focused only on symbiotic-specific clusters whose proteins are not
139 clustered in aposymbiotic cells. Second, we expected that most PV proteins would have higher
140 abundance in symbiotic cells, as aposymbiotic cells do not possess this structure. Third, we
141 expected that the PV cluster should contain a significant proportion of membrane-related proteins.
142 By analyzing all clusters between these two cell types, we found that cluster 18 in symbiotic cells
143 represents a unique cluster, in which proteins were not clustered or were partially clustered in
144 several different groups in aposymbiotic cells (Fig. 3A). Cluster 18 contains 109 protein groups in
145 symbiotic cells. All 109 protein groups are also detected in the aposymbiotic proteome; however,
146 they are dispersed across multiple different clusters rather than forming a single coherent group
147 (Fig. 3A), consistent with the notion that PV proteins are pre-existing host proteins that are
148 relocalized upon symbiosis establishment. We examined whether other clusters also showed
149 differential patterns between symbiotic and aposymbiotic cells. While some clusters exhibited
150 minor differences in protein membership, cluster 18 was the only one that simultaneously met all
151 three of our selection criteria, making it the strongest PV candidate. Moreover, their protein
152 abundance in symbiotic cells is significantly higher than that in aposymbiotic cells (Fig. 3B, C).
153 The proteins in cluster 18 were enriched for GOCC terms including cytoplasmic vesicle
154 membrane, clathrin coat, and endosome membrane (Fig. 2A and data file S3C), which is also
155 consistent with the characteristics of PVs (*27*). Together, these data suggest that cluster 18 is a
156 strong perialgal vacuole candidate.
157 To experimentally validate the cellular localization of proteins in cluster 18, we performed
158 immunostaining of symbiotic cells with an antibody against one of the cluster 18 proteins,
159 vacuolar protein sorting 4A (VPS4A). The result showed that VPS4A surrounds the algal cell
160 wall inside the symbiotic cell (Fig. 3D), consistent with the expected localization of PVs. In
161 contrast, no VPS4A signal above background was detected in aposymbiotic cells (fig. S3),
162 consistent with the dispersal of cluster 18 proteins across multiple subcellular compartments in
163 aposymbiotic cells (Fig. 3A) and the absence of perialgal vacuole membranes on which VPS4A
164 could concentrate into detectable ring structures. Importantly, in symbiotic cells, VPS4A rings
165 were observed exclusively around endosymbiotic *Chlorella* cells and were absent from ingested
166 food algae (*Chlorogonium capillatum*) undergoing digestion in digestive vacuoles (fig. S3, yellow

167 arrows), demonstrating that VPS4A ring formation is specific to the perialgal vacuole membrane
168 and does not occur on digestive vacuole membranes. In the following analyses, we selected
169 several cluster 18-specific proteins as the PV markers for supervised clustering.
170
171 **A Spatial proteome maps of symbiotic and aposymbiotic *P. bursaria***
172 To construct spatial maps, marker proteins that collectively represent the cell's compartments
173 were first required. Since *P. bursaria* is less well studied, the initial marker set was developed
174 based on ortholog localization information from previous studies (*20, 33*) and guided by
175 HDBSCAN clustering (fig. S2B and data file S4A, see Methods for details). Consequently, we
176 selected a total of 252 maker proteins that defined 14 cellular compartments, including the
177 cytosol, proteasome, ribosome, peroxisome, endoplasmic reticulum (ER), Golgi, plasma
178 membrane, nucleus, lipid droplet, basal body, mitochondria, phagolysosome, trichocyst, and
179 potential perialgal vacuole. These cell-compartment markers exhibited distinct fractionation
180 profiles (Fig. 4A and figs. S4 and S5), indicating that the different compartments were well
181 separated.
182 Next, we used the total proteins (n = 10255) that overlapped between aposymbiotic and
183 symbiotic cells for spatial proteome characterization. Our mass spectrometry data were globally
184 normalized and then analyzed using support vector machine (SVM)-based supervised learning,
185 which computes the probability of a protein belonging to one of our pre-defined subcellular
186 compartments by finding the best boundary that separates data points into different classes and
187 maximizing the margin (*34*). Each protein was probabilistically assigned to a compartment.
188 Allocations represent the most probable compartmental localization of each protein in the dataset.
189 To increase stringency, we retained only protein assignments with medium or higher confidence
190 (i.e., probability > 0.5, see Methods) for further analysis. In total, we classified the subcellular
191 localizations of 4175 and 3387 proteins in the symbiotic and aposymbiotic cells, respectively,
192 representing more than one-third of the identified *P. bursaria* proteome (Fig. 4B, fig. S6, and data
193 file S4B,C). Among the classified proteins, 1237 have not previously had functional annotation.
194 Our data provide additional information on their potential functions.
195 When we projected the 33-dimension protein profiling dataset (from 33 fractions of three
196 replicates, fig. S7 and data file S1B) of classified proteins into two dimensions by t-distributed
197 stochastic neighbor embedding (t-SNE), we found that the proteins of different cellular
198 compartments formed discrete clusters (Fig. 4C and data file S5A,B), indicating that our analysis
199 can clearly distinguish proteins displaying differential localization patterns. In addition, the

distribution of individual subcellular compartments showed highly overlapping patterns with clusters of similar functions in our unsupervised clustering data (Fig. 2 and data file S3A,B).

We further inspected the SVM classification using an alternative localization annotation. Classified proteins from each subcellular localization were subjected to GOCC term enrichment analysis. (Fig. 5A and data file S4D,E, and F). The results revealed consistent and sensible patterns across all cellular compartments in both symbiotic and aposymbiotic cells. For example, trichocyst matrix was enriched with "extracellular membraneless organelle", proteasome with "proteasome complex", basal body with "axoneme" and "motile cilium", and mitochondria with "mitochondrial inner membrane". Notably, although the PV is a symbiosis-specific structure, a small number of proteins with PV-like fractionation profiles were classified into this compartment in aposymbiotic cells (Fig. 5A), likely representing pre-existing endosomal membrane proteins that are reorganized to form the PV upon establishment of endosymbiosis. These analyses demonstrate a high resolution of diverse subcellular compartments with relevant biochemical protein features.

Comparison of spatial proteomes with deep learning predictions

Since *P. bursaria* cells cannot be genetically manipulated and only a few proteins have been experimentally characterized based on their cellular localization, it is almost impossible to systematically validate our proteomics data. Nonetheless, a pre-trained protein language model, DeepLoc 2.0, has been shown to predict protein subcellular localization with reasonable accuracy (*35*) across several model organisms. We compared our localization data with DeepLoc predictions (data file S6A,B). A large proportion of the proteins assigned to the ER and mitochondria in our experiments were consistently predicted by DeepLoc to localize to those organelles, respectively (Fig. 5B). The majority of nuclear proteins predicted by DeepLoc were also found in a group mapping to the nucleus. Since the training organisms are evolutionarily distant from *P. bursaria*, the accuracy of DeepLoc predictions for ciliate-specific proteins may be reduced. Moreover, approximately one-third of the *P. bursaria* proteome lacks reasonable orthologs in databases of other model organisms.

Interestingly, Deeploc predicted many trichocyst- and phagolysosome-associated proteins as being extracellular. Trichocysts are secretory organelles found in ciliates and some flagellate protists (*36*). They comprise a cavity and long threads of trichocyst proteins that can be released extracellularly in response to external stimuli, such as the detection of predators (*37*). Phagolysosomes are formed by the fusion of phagosomes with lysosomes after phagocytosis. Although phagolysosomes are primarily involved in degrading food and debris, they may also be

234 used to degrade secreted proteins or exosomes engulfed by phagocytosis or endocytosis (*38*).
235 Further studies of the "extracellular" nature of trichocyst and phagolysosome proteins are needed
236 to understand this finding.
237 In addition to DeepLoc, we applied a deep-learning protein language model-based
238 algorithm, DeepTMHMM, to predict potential transmembrane proteins (*39*). The analysis showed
239 that proteins assigned to the plasma membrane, lipid droplet, Golgi apparatus, and endoplasmic
240 reticulum (ER) contained a higher proportion of transmembrane proteins (fig. S8 and data file
241 S6A,B), consistent with their membrane-bound or membrane-trafficking roles. In contrast,
242 proteins assigned to the perialgal vacuole showed a comparatively low proportion of predicted
243 transmembrane proteins. However, we note that the high proportion of predicted transmembrane
244 proteins among lipid droplet-assigned proteins likely reflects co-fractionation of ER-resident
245 proteins with lipid droplets, as these two compartments are physically connected through
246 membrane bridges (*40, 41*). Lipid droplets are bounded by a phospholipid monolayer rather than a
247 bilayer (*42*), and many LD-associated proteins use hairpin or monotopic membrane anchors that
248 topology predictors cannot distinguish from true transmembrane helices (*43*). Indeed, recent
249 benchmarking of spatial proteomics methods has shown that lipid droplets are among the most
250 challenging compartments to resolve in density gradient-based approaches, with standard
251 classifiers achieving near-zero performance for this organelle (*44*). Therefore, the SVM-assigned
252 lipid droplet proteome should be considered a broad candidate set that includes both genuine LD
253 proteins and ER-derived co-fractionating proteins. Together, the DeepLoc and transmembrane
254 protein predictions are consistent with the SVM-based classification results. In addition to helping
255 decipher the possible functions of unknown proteins, our comprehensive localization maps
256 enabled us to investigate the physiological changes that occur during the establishment of
257 endosymbiosis.
258
259 **Several cellular compartments are reorganized in symbiotic cells**
260 Given that symbiotic *P. bursaria* cells reorganize their cytoplasm to accommodate hundreds of
261 endosymbiotic algae, we expected that the localization of certain proteins might be altered to
262 accommodate them. Comparing the spatial proteome maps between symbiotic and aposymbiotic
263 cells (Fig. 6A), we observed a dramatic change in protein numbers in the perialgal vacuole (PV),
264 lipid droplet, Golgi, and peroxisome, suggesting that these organelles were potentially
265 reorganized during endosymbiosis. To investigate this observation, we performed Gene Ontology
266 Biological Process (GOBP) enrichment analysis of symbiotic cell-specific proteins in these
267 organelles (data file S7A).

268 The perialgal vacuole is a symbiotic cell-specific compartment that protects algal cells from
269 lysosomal degradation in *P. bursaria* cells (*45*). In the symbiotic spatial map, we observed that
270 the PV cluster is located near the phagolysosome cluster (Fig. 4D). Several lysosome-related
271 biological processes are also enriched among symbiotic cell-specific PV proteins (fig. S9 and data
272 file S7A). The enrichment of lysosomal functions in PV proteins is consistent with the hypothesis
273 that PVs may regulate symbiont load through selective digestion of excess endosymbionts.
274 Notably, a glycogen catabolic process term was also enriched among PV proteins, suggesting
275 potential carbohydrate exchange between the host and endosymbionts at the PV interface.
276 Moreover, many processes related to transport and organelle organization are enriched, consistent
277 with the expected functions of PVs in exchanging nutrients and wastes between the host and
278 endosymbionts.
279 Lipid droplets regulate intracellular lipid storage, transport, and metabolism (*46*). They are
280 highly dynamic structures, interacting with various organelles (including ER, Golgi,
281 mitochondria, lysosomes, and peroxisomes) to exchange proteins and lipids, and acting as vital
282 hubs of cellular metabolism (*47*). An enrichment analysis of lipid droplet proteins specifically in
283 symbiotic cells revealed enrichment for many pathways involved in lipid metabolism, organelle
284 organization, vesicle trafficking, and ion transport (fig. S9). These pathways are all related to
285 various functions of lipid droplets, indicating that the functions of lipid droplets may shift in
286 symbiotic cells and be involved in the host-symbiont interaction. The enrichment of lipid
287 phosphorylation and lipid transport processes in symbiotic cell-specific lipid droplet proteins
288 suggests active lipid remodeling, possibly to support the metabolic demands of maintaining
289 hundreds of endosymbiotic algae.
290 Recent studies have highlighted the pivotal role of Golgi-associated mechanisms in
291 regulating symbiotic relationships, as some proteins targeting to the endosymbiont need to be
292 mediated by the Golgi (*48, 49*). In our enrichment analysis of Golgi proteins, we observed that
293 terms related to vesicle trafficking, protein transport, organelle organization, and cellular
294 localization were enriched (fig. S9). The similarity between the enriched terms in symbiotic cell-
295 specific PV, lipid droplet, and Golgi proteins suggests that these cellular compartments may be
296 reorganized to form a central architecture that supports the host-symbiont interaction.
297 Peroxisomes, traditionally known for their roles in lipid metabolism and reactive oxygen
298 species (ROS) detoxification, are now recognized to respond to pathogens and regulate immune
299 pathways (*50, 51*). However, some viruses and bacteria have evolved mechanisms to hijack this
300 plasticity, remodeling the metabolic output to promote their proliferation (*52, 53*). We observed
301 enrichment in lipid metabolism, stress response, and signaling pathways (fig. S9), which represent

302 the general functions of peroxisomes. The enrichment of oxidative stress response pathways in
303 symbiotic cell-specific peroxisomal proteins is particularly noteworthy, as photosynthetic activity
304 of the endosymbiotic algae is expected to generate elevated levels of reactive oxygen species in
305 the host cytoplasm, necessitating enhanced antioxidant capacity. More experiments are needed to
306 understand the contribution of peroxisomes to symbiotic *P. bursaria* cells.
307 Previous studies have suggested that mitochondria are involved in the endosymbiosis of
308 ciliates (*26, 54*). It prompts us to examine the mitochondrial proteins more carefully.
309 Interestingly, GO terms related to nucleotide metabolism and stress response were enriched in
310 symbiotic cell-specific mitochondrial proteins, suggesting that mitochondria were under stress
311 (data file S7A). A previous microscopic study showed that symbiotic *P. bursaria* cells contained
312 fewer mitochondria than aposymbiotic ones (*26*). Surprisingly, our total lysate proteomes
313 revealed that the abundance of mitochondrial proteins in symbiotic cells was significantly higher
314 than that in aposymbiotic cells (fig. S10). Since the strain backgrounds are different between
315 these two experiments, it remains to be determined whether the discrepancy is due to the
316 difference in genetic background or methodology.
317
318 **Inhibition of lipid metabolism reduces the number of endosymbionts**
319 Our spatial proteomics data, combined with enrichment analysis, revealed that lipid droplets
320 undergo a dramatic compositional change in symbiotic cells. Consequently, we stained the cells
321 with the lipid droplet dye LipidSpot to examine them by confocal microscopy. We observed that,
322 in individual symbiotic cells, hundreds of tiny lipid droplets seemed to interact with the
323 endosymbiotic algae (Fig. 6B). The total LipidSpot fluorescence intensity of lipid droplets in
324 symbiotic cells was higher than that in aposymbiotic cells (approximately 1.5-fold increase, Fig.
325 6C). Consistent with this observation, our total lysate proteomics data showed that the protein
326 abundance of several enzymes involved in the biosynthesis of triacylglycerol (TAG), a major core
327 component of lipid droplets, was increased in symbiotic cells (data file S2 and fig. S11).
328 Next, we used transmission electron microscopy (TEM) to examine the relationship
329 between lipid droplets and endosymbiotic algae in greater detail. Indeed, the lipid droplets were
330 localized near most algae, with some of them (2.4 ± 1.3 lipid droplets per algal cell TEM image, n
331 = 40) being directly attached to the perialgal vacuole (PV) membrane surrounding individual algal
332 cells (Fig. 6D). Together, these observations indicate that the reorganization of lipid droplets in
333 the symbiotic cells may play a role in the host cells' interactions with their endosymbionts.

334 We investigated whether lipid droplets are crucial for maintaining endosymbionts using two
335 lipid metabolism inhibitors, H89 and T863. H89 blocks protein kinase A and other kinases,
336 leading to an imbalance between lipolysis and lipogenesis (*55, 56*). T863 can reduce triglyceride
337 synthesis and lipid droplet formation by inhibiting diacylglycerol acyltransferase 1 (DGAT1)
338 (*57*). We treated symbiotic cells with a mild dose of H89 (1 μM) or T863 (10 μM), which did not
339 affect host survival. Application of these drugs reduced the number of lipid droplets in symbiotic
340 cells (Fig. 7A), and the treatments negatively influenced the number of endosymbionts in host
341 cells (Fig. 7B and 7C). Compared with untreated controls, H89 treatment reduced total algal
342 fluorescence by approximately 40%, whereas T863 treatment reduced it by approximately 30%
343 (Fig. 7C). Together, our data indicate that lipid droplets play a crucial role in endosymbiosis.
344

345 **Discussion**

346 *P. bursaria* represents a unique position in the evolution of endosymbiosis in unicellular
347 eukaryotes. In this study, the proteome of two types of *P. bursaria* cells (symbiotic and
348 aposymbiotic) was mapped to 14 subcellular compartments. The fidelity of the classification was
349 verified through multiple orthogonal analyses. Moreover, we identified an important symbiotic
350 cell-specific compartment, the perialgal vacuole, and experimentally validated the localization of
351 one of the predicted PV proteins. Further investigation of the PV proteins will open up
352 opportunities for functional characterization of PVs. We note that while other HDBSCAN clusters
353 also showed minor differences between symbiotic and aposymbiotic cells, cluster 18 was the only
354 one that simultaneously satisfied all three selection criteria (symbiotic-specific clustering, higher
355 protein abundance, and membrane protein enrichment). Notably, the GOCC enrichment of cluster
356 18 proteins also included food vacuole and phagolysosome terms, consistent with the established
357 model that the PV membrane originates from the host digestive vacuole membrane (*27*), implying
358 that many PV proteins are pre-existing phagocytic membrane components retained during
359 endosymbiosis establishment. Additionally, myosin complex proteins were enriched in cluster 18,
360 suggesting active cytoskeletal remodeling at the PV membrane, a feature that parallels the
361 cytoskeletal remodeling function identified in the cnidarian symbiosome membrane proteome
362 (*58*). The enrichment of lysosomal functions among PV proteins supports the hypothesis that PVs
363 may participate in symbiont load control through selective digestion of excess algae, a mechanism
364 that would help maintain a stable host-endosymbiont ratio.
365 The low proportion of DeepTMHMM-predicted transmembrane helices among the classified PV
366 proteins is not inconsistent with enrichment of trafficking and membrane-remodeling factors at

367 the PV, because many proteins that function on endosomal and vacuolar membranes are
368 peripheral rather than integral membrane proteins. Rab GTPases, key coordinators of vesicle
369 identity and trafficking, are prenylated membrane-associated proteins that lack transmembrane
370 helices (*59*). Likewise, ESCRT components are peripheral membrane-associated factors, and
371 VPS4A is a soluble AAA-ATPase that is recruited transiently to ESCRT-III assemblies on
372 membranes rather than spanning the membrane (*60, 61*). Accordingly, the absence of canonical
373 transmembrane helices does not exclude functional association with the PV. DeepTMHMM is a
374 useful screening tool, but negative predictions should be interpreted cautiously for highly
375 divergent proteins from non-model organisms and ideally integrated with orthology, domain
376 content, localization, and experimental data.

377 The subcellular localization datasets are particularly powerful when comparing different
378 physiological conditions. Our results revealed that proteins assigned to lipid droplets were
379 changed dramatically between symbiotic and aposymbiotic cells. Moreover, lipid droplets
380 underwent morphological changes and often attached to PVs in symbiotic cells (Fig. 6). Inhibition
381 of lipid droplet formation resulted in a significant reduction in endosymbiont numbers, with H89
382 and T863 treatments reducing total algal fluorescence by approximately 40% and 30%,
383 respectively (Fig. 7). These data suggest that lipid droplets play a role in maintaining
384 endosymbionts. Although the exact boundaries of the lipid droplet proteome are difficult to
385 delineate due to the inherent challenges of resolving lipid droplets in density gradient-based
386 spatial proteomics (*44, 62, 63*), the involvement of lipid droplets in endosymbiosis does not rely
387 on the computational assignments alone. Our confocal microscopy data independently
388 demonstrate altered lipid droplet morphology and increased LipidSpot fluorescence in symbiotic
389 cells, while TEM imaging directly reveals physical attachment of lipid droplets to the perialgal
390 vacuole membrane. Moreover, the upregulation of TAG biosynthesis enzymes in total lysate
391 proteomics confirms elevated lipid metabolism in symbiotic cells at the protein abundance level.
392 Crucially, two pharmacological inhibitors targeting distinct steps of lipid metabolism, H89, which
393 disrupts kinase-mediated lipolysis regulation, and T863, which blocks DGAT1-dependent
394 triglyceride synthesis, both independently reduced lipid droplet numbers and endosymbiont load.
395 This convergence of imaging, biochemical, and functional evidence strongly supports a role for
396 lipid droplets in maintaining endosymbiosis.

397 Lipid droplets have been observed in several different symbiotic systems and are suggested
398 to perform diverse functions. Symbiotic corals convert lipids or low molecular weight
399 carbohydrates released from dinoflagellate endosymbionts to form gastrodermal lipid bodies (*64,*

400 *65*). The lipid composition of lipid bodies varies depending on host physiology (*66*). These lipid
401 droplets likely serve as nutrient storage sites that reorganize the nutrients acquired from the
402 endosymbiont. Nonetheless, they may have additional biological functions that remain to be
403 investigated. It was also observed that endosymbiotic algae in *P. bursaria* enhanced carbon
404 fixation efficiency and accumulated more lipid droplets than free-living algae (*67*). It was
405 suggested that these lipid droplets could serve as an energy source for the host. In a symbiotic
406 bacterial system, *Saccharibacteria* induce their host cells to form lipid droplets (*68*). The
407 accumulation of lipid droplets enables host cells to become more tolerant of environmental stress,
408 suggesting a protective function of lipid droplets. If the function of lipid droplets in *P. bursaria* is
409 similar to the abovementioned cases, the reduced endosymbionts observed in lipid metabolism-
410 compromised cells are probably due to an indirect effect caused by imbalanced nutrient
411 metabolism or weakened host physiology.

412 Lipid droplets were also observed to play a crucial role in host-pathogen interactions.
413 Pathogens, including viruses, bacteria, and eukaryotic parasites, can manipulate host lipid
414 metabolism and exploit lipid droplets as nutrient sources or as platforms for viral replication (*69*).
415 For example, mammalian cells infected by the protozoan *Toxoplasma* display increased numbers
416 of lipid droplets (*70*). These newly formed lipid droplets attach to the parasitophorous vacuole
417 containing *Toxoplasma* cells, allowing the parasites to utilize the nutrients for their own
418 reproduction (*71*). Similarly, lipid droplets in *P. bursaria* cells may facilitate nutrient uptake by
419 the endosymbiotic algae from the host. In another ciliate symbiotic system, the host and
420 endosymbionts have coevolved a mechanism to balance resource allocation (*54*). Whether
421 remodeled lipid droplets in symbiotic *P. bursaria* cells are used to support the algal growth, as
422 observed in the *Toxoplasma* case, remains to be established.

423 Since the perialgal vacuole is a membranous structure, lipid droplets may provide essential
424 components for generating or maintaining PVs. Inside *P. bursaria*, a PV membrane surrounds
425 each algal cell, and this membranous structure needs to divide and reorganize each time the algal
426 cells reproduce. If PV structures become compromised, it would likely result in unstable
427 endosymbiosis. Lastly, lipid droplets may serve as a signal-exchange hub between the host and
428 endosymbionts, with their disruption meaning impaired communication between the two
429 interacting partners, potentially prompting digestion of the endosymbionts.

430 This study establishes a molecular framework for understanding how a ciliate host
431 reorganizes its cellular architecture to accommodate endosymbiotic algae; nonetheless, several
432 aspects invite further investigation. *P. bursaria* is not currently amenable to genetic manipulation,

433 so experimental validation relied on immunolocalization and pharmacological approaches.
434 Among the identified PV candidate proteins, VPS4A is the only one directly confirmed by
435 microscopy, and expanding this set is an important priority for future work. The spatial
436 proteomics data represent a static snapshot of two physiological states and do not capture
437 dynamic protein redistribution during symbiosis establishment or algal division cycles. H89 and
438 T863 have broad cellular targets; while concordant results from two mechanistically distinct
439 inhibitors strengthen our conclusions, indirect effects on the endosymbionts cannot be fully
440 excluded. Finally, this study examined a single laboratory strain, and whether these findings
441 generalize to other *P. bursaria* strains or related ciliate-alga partnerships remains to be
442 determined.
443 The contribution of lipid droplets to maintaining a mutualistic endosymbiosis adds a new
444 dimension to the already complex functions of these organelles. Peroxisomal proteins involved in
445 oxidative stress response are enriched in symbiotic cells, suggesting that peroxisomes help
446 mitigate reactive oxygen species generated by photosynthetic endosymbiont activity. Together,
447 these findings demonstrate that even unicellular organisms can substantially reorganize their
448 cellular compartments in response to physiological demands. The comparative spatial proteome
449 datasets reported here provide a resource for future studies on ciliate biology and the molecular
450 basis of endosymbiosis.
451
452 **Materials and Methods**
453 **Experimental Design**
454 This study generated comparative spatial proteome maps of symbiotic and aposymbiotic
455 *Paramecium bursaria* cells to identify organelles and proteins reorganized during endosymbiosis.
456 Cells were lysed by nitrogen cavitation and subcellular compartments separated by differential
457 centrifugation, followed by LC-MS/MS proteomics. Protein abundance profiles were analyzed by
458 unsupervised clustering and supervised SVM classification against curated marker proteins to
459 assign subcellular localizations. Total lysate proteomics was performed in parallel to compare
460 protein abundances between cell types. The functional role of lipid droplets in endosymbiosis was
461 assessed by confocal microscopy, transmission electron microscopy, and pharmacological
462 perturbation using lipid metabolism inhibitors.
463
464 **Strains and cell culture conditions**

465 All the *P. bursaria* cells used in the study belong to the DK2 strain (*19*). *P. bursaria* cells were
466 cultured in 12 mM sodium acetate, 0.5% yeast extract with modified Dryl's buffer (2 mM sodium
467 citrate, 1 mM NaH_2PO_4/Na_2HPO_4 and 1.5 mM $CaCl_2$) and fed with *Chlorogonium capillatum*
468 (National Institute for Environmental Studies, Japan, strain #NIES-3374) cells every five days.
469 The cell cultures were kept at 23 °C with a light-to-dark cycle of 12 h:12 h. To obtain
470 aposymbiotic *P. bursaria* strains, green symbiotic cells were treated with 100 μg/ml of methyl
471 viologen dichloride hydrate (Paraquat dichloride, Cat #856177, Sigma-Aldrich, MA, USA) for
472 approximately one week in a light-to-dark cycle of 12 h:12 h (*72*). The aposymbiotic cells were
473 maintained under low-light conditions.
474 For the inhibitor treatment experiments, 20 ml of symbiotic *P. bursaria* cells (1000
475 cells/ml) were treated with different concentrations of H89 (Cat. # HY-15979, MedChemExpress,
476 NJ, USA) or T863 (Cat. # HY-32219, MedChemExpress) to test their viability and growth. We
477 used 1 μM of H89 and 10 μM of T863 in the final experiment since these drug concentrations did
478 not have any apparent deleterious effects on *P. bursaria* cells. After two weeks of treatments, we
479 observed the morphology of the host lipid droplet and symbiotic algae by confocal microscopy.
480
481 **Total lysate preparation and subcellular compartment fractionation**
482 For each biological replicate of the total proteome experiment, 1×10^5 *P. bursaria* cells
483 (approximately 0.5 L of the culture volume) were harvested on an 11-μm-diameter nylon mesh
484 sieve after removing cell debris with cheesecloth. The cells were washed on the nylon mesh with
485 Dryl's solution and then transferred to 1.5-ml tubes. The cells were resuspended in 1 ml of UTU
486 buffer (6 M urea, 2 M thiourea, 100 mM Tris, 2.5 mM DTT, 5 mM EDTA-KOH [pH 8.0], 1
487 mM/2 mM PMSF/SHAM, and 1× protease inhibitor cocktail). After centrifugation at 12,000 × g,
488 the supernatant was collected for LC-MS analysis.
489 For each biological replicate of the subcellular fractionation experiment, 4×10^5 *P. bursaria*
490 cells (around 2 L of the culture volume) were harvested from an 11 μm-diameter nylon mesh
491 sieve after removing cell debris using cheesecloth. The cells were washed on the nylon mesh with
492 Dryl's solution before being decanted into 15 ml tubes. Then, the cells were resuspended in lysis
493 buffer (10 mM HEPES-KOH [pH 7.5], 2 mM EDTA-KOH [pH 8.0], 2 mM magnesium, 1 mM/2
494 mM PMSF/SHAM, 250 mM sucrose and 1× protease inhibitor cocktail) and lysed using a
495 nitrogen cavitation bomb. The cavitation bomb was pressurized to 300 psi and incubated for 20
496 min before slowly releasing the pressure.

497 The lysate was then differentially centrifuged at 300 x *g* for 3 min, 1000 x *g* for 10 min,
498 3000 x *g* for 10 min, 5000 x *g* for 10 min, 9000 x *g* for 15 min, 12000 x *g* for 15 min, 15000 x *g*
499 for 15 min, 30000 x *g* for 20 min, 79000 x *g* for 43 min, and 120000 x *g* for 45 min. After each
500 centrifugation, the pellet was collected and resuspended in UTU buffer and stored at -80 ºC. After
501 the 12000 x *g* centrifugation step, we added acetone to the supernatant to precipitate the protein
502 overnight at -20 ºC. Protein concentration was determined by Bradford assay.
503 Fractions (5ug loading) were analyzed by Western blotting using a standard method with
504 antibodies against the protein marker. The antibody against a *P. bursaria* mitochondrial protein
505 (ubiquinol-cytochrome c reductase complex protein) was generated by inoculating a rabbit with a
506 synthesized peptide. The antibody was diluted to 1μg/ml for immunoblotting. Protein bands were
507 visualized via the chemiluminescence detection using Western Lightning Plus-ECL (PerkinElmer,
508 CT, USA).
509
510 **Sample preparation and LC-MS analysis**
511 Protein digestion in the S-Trap microcolumn (ProtiFi, NY, USA) was performed according to a
512 previous report (*73*). In brief, 5 μg of protein in lysis buffer was reduced and alkylated using
513 10 mM Tris(2-carboxyethyl) phosphine hydrochloride and 40 mM 2-chloroacetamide at 45 °C for
514 15 min. A final concentration of 5.5% (v/v) phosphoric acid (PA), followed by a six-fold volume
515 of binding buffer (90%, v/v, MeOH in 100 mM triethylammonium bicarbonate (TEAB)), was
516 next added to the protein solution. After gentle vortexing, the solution was loaded into an S-Trap
517 microcolumn. The solution was removed by spinning the column at 4,000 x *g* for 1 min. The
518 column was washed three times with 150 μl binding buffer. Finally, 20 μl of digestion solution
519 containing 200 ng Lys-C and trypsin in 50 mM TEAB was added to the column and incubated at
520 47 °C for 2 h. Each digested peptide was eluted using 40 μl of three buffers consecutively: (1)
521 50 mM TEAB; (2) 0.2% (v/v) formic acid (FA) in H_2O; and (3) 50% (v/v) acetonitrile (standard
522 elution). Elution solutions were collected in a tube and dried under a vacuum. A total of 500 ng
523 peptides was loaded into an Evotip and then the Evotip was placed into an Evosep One system
524 (Evosep Biosystems, Odense, Denmark) coupled to a timsTOF HT mass spectrometer (Bruker
525 Daltonics, MA, USA).
526 Indexed retention time peptides (iRT) (KI-3002-2, Biognosys, Schlieren, Switzerland) were
527 dissolved in 50 μl of 0.1% (v/v) FA with 3% (v/v) ACN to achieve a 10× stock solution. The
528 stock solution was then diluted 10-fold. Dried peptides were reconstituted in 200 μl of 0.1% (v/v)

529 trifluoroacetic acid. Then, 20 µl of samples and 10 µl of 1× iRT solution were loaded onto
530 EvoTips and analyzed using the same Evosep One system.
531 Eluting peptides were separated analytically using the 30 SPD method on an Evosep
532 Performance column (15 cm x 150 µm ID, 1.5 µm, EV1137; Evosep) at 40 °C within a Captive
533 Spray source (Bruker Daltonics), equipped with a 20 µm emitter (ZDV Sprayer 20, Bruker
534 Daltonics), followed by dia-PASEF mode analysis. For dia-PASEF, the instrument firmware was
535 adapted to perform data-independent isolation of multiple precursor windows within a single
536 TIMS frame. An optimized dia-PASEF scheme was applied that targeted +2 and +3 ions in a two-
537 window method. Sixteen of these scans (resulting in 32 windows, each of 25-Da window size)
538 covered an m/z range of 400 to 1200. Each dia-PASEF cycle comprised an MS1 survey frame,
539 followed by 16 dia-PASEF frames, with this setup resulting in a total cycle time of 1.8 s.
540

541 **Data-independent acquisition (DIA) analysis**

542 DIA data signal extraction and quantification were performed with an analysis pipeline in
543 Spectronaut (Biognosys, v18.7, https://biognosys.com/software/spectronaut/) using a standard
544 setting with Carbamidomethylation (Cys) specified as a fixed modification, oxidation (Met), and
545 N-terminal acetylations specified as variable modifications. We selected dynamic retention time
546 prediction with local regression calibration. Interference correction for the MS and MS2 levels
547 was enabled. The FDR was set to 1% at peptide precursor and protein levels using scrambled
548 decoy generation and a dynamic library size fraction set at 0.1. MS2-based quantification was
549 used, enabling local cross-run normalization. Peptide precursor abundances were measured by the
550 sum of fragment ion peak areas and peptide grouping was performed based on modified peptides.
551 Protein-level quantification was performed against the spectrum library generated *in silico* by
552 Spectronaut with standard settings and a stripped peptide sequence area obtained from the mean
553 precursor area.
554

555 **Data processing and assessment of proteomics depth**

556 For label-free quantitation (LFQ) maps, Spectronaut already globally normalizes intensities,
557 hence no further normalization was required. Proteins not identified in all replicates were
558 removed. Three biological replicates were performed for each cell type. Proteomic differences
559 were evaluated for statistical significance ($P<0.05$) by Student's t-tests and corrected for multiple
560 testing using the Benjamini-Hochberg correction. Normalization (0-1) of each fractionation
561 profile was performed by summing the intensities across all fractions and dividing each intensity

562 by the profile sum. Proteomics depth was assessed by counting protein groups or proteins
563 identified in one or all replicates.
564
565 **Unsupervised clustering**
566 Normalized protein abundance profiles from 33 fractions of three replicates were concatenated
567 and analyzed using hierarchical density-based spatial clustering of applications with noise
568 (HDBSCAN) (*30*). The algorithm generated 20 and 19 clusters in symbiotic and aposymbiotic
569 cells, respectively. The HDBSCAN algorithm is available in Python Scikit-learn (*33*).
570
571 **Marker protein curation and support vector machine (SVM) analysis**
572 To generate the subcellular compartment marker protein list, we first examined the marker
573 proteins identified in *Paramecium tetraurelia* (*74*) by manually reviewing the literature and
574 InterProScan annotations. Next, we used OrthoFinder (*75*) to identify orthologous markers in the
575 *P. bursaria* genome. These were then further selected guided by HDBSCAN unsupervised
576 clustering. These marker proteins were inspected for their protein abundance distribution profiles
577 and checked for their deviation from the cluster using a 5-fold cross-validation function provided
578 in Scikit-learn (*33*). Only the marker proteins present in all compared datasets were included, and
579 identical SVM parameters were used.
580 Classification of unlabeled proteins was performed using SVM. Based on SVM, we
581 achieved a prediction accuracy (F1-score) of 95.2% for symbiotic and 91.5% for aposymbiotic
582 cells (fig. S5a). Finally, we established a list of manually curated proteins defining 14 subcellular
583 compartments (cytosol, proteasome, ribosome, peroxisome, ER, Golgi, plasma membrane,
584 nucleus, lipid droplet, basal body, mitochondrion, phagolysosome, PV membrane and trichocyst)
585 (data file S4A). To further evaluate the performance of our subcellular compartment maps, their
586 power to predict protein localization was assessed using quality-filtered and normalized (0-1) data
587 with full replicate coverage.
588 For supervised classification, the marker proteins covering 14 subcellular localizations were
589 used by SVM to assign all other proteins to the organellar cluster. Machine learning was
590 conducted using the functionality-based command provided in Scikit-learn (*33*). SVM enables
591 selection of marker classes, definition of a hold-out test set, automated hyperparameter
592 optimization and, finally, SVM training and prediction. During training, the parameters C and
593 gamma of the radial basis function were optimized via an iterative grid search, with 5-fold cross-
594 validation. At each grid point, SVMs were run on each loaded dataset before identifying the

optimum for summed accuracy across datasets. Finally, we confirmed analytical performance using Q-Sep (*76*), which quantifies the separation between a pair of predicted protein sets by comparing intra-group and inter-group distances (fig. S5b and data file S8A,B).

For prediction, the SVM was fitted using the training set and 5-fold cross-validation to convert the raw SVM scores into probabilities. Proteins were then assigned to the best-fitting organelle model and divided into confidence classes based on probability: >0.9, very high confidence; >0.8, high confidence; >0.5, medium confidence; >0.4, low confidence; <0.4, best-guess assignment (*77*). In our dataset, probabilities lower than 0.5 were labeled as unknown. For the hold-out test set, a misclassification matrix was derived to calculate global marker prediction recall (proportion of correctly predicted markers to the total number of markers), organelle-specific recall (proportion of markers correctly assigned to the cluster), and organelle-specific precision (ratio of markers correctly assigned to the number of all markers assigned to the cluster). The harmonic mean of recall and precision (F1 score) was used as the primary readout for SVM performance.

t-SNE (t-distributed stochastic neighbor embedding) visualization

t-SNE was used to reduce dimensionality and visualize data. For t-SNE, the preprocessed data were embedded into two dimensions using a perplexity of 60 and extract gradient calculation for a maximum of 1000 iterations. The computed coordinates were recorded and used to obtain the two-dimensional data projection presented herein.

Protein annotation and GO/KEGG enrichment analysis

GO terms and KEGG terms were predicted by InterProScan (*78*), the String database 12 (*79*), DeepFRI (*80*), and Pannzer 2 (*81*). Fisher's exact tests were applied to the annotation terms. The resulting *P* values were corrected for multiple hypotheses using the Bonferroni correction, and a cutoff of 5% FDR was applied (*82*).

DeepLOC and DeepTMHMM predictions

For subcellular localization, protein feature annotations were predicted using DeepLoc 2.0 (*35*). Transmembrane span prediction was performed using DeepTMHMM (*39*) in *P. bursaria* annotated protein sequences.

Confocal microscopy

628 *P. bursaria* cells were subjected to various staining procedures to visualize lipid droplets, cell
629 walls, and protein localization. All samples were prepared under consistent fixation and imaging
630 conditions to ensure comparability across experiments. For lipid droplet staining, cells were
631 similarly fixed with 4% formaldehyde for 10 minutes and stained with LipidSpot dye (1000X
632 dilution; Cat. # 70065-T, Biotium, CA, USA) for 30 minutes at room temperature. Fluorescence
633 signals were detected using a confocal microscope with an excitation wavelength of 440 nm and
634 an emission wavelength of 585 nm.

635 For immunofluorescence detection of VPS4A, cells were fixed in 4% paraformaldehyde in
636 PBS using rapid microwave irradiation (PELCO 3451 Laboratory Microwave System, Ted Pella)
637 with the ColdSpot set to 10 °C. The program consisted of three cycles (1 min on - 1 min off - 1
638 min on - 1 min off - 1 min off - 1 min on) at 250 W. After fixation, samples were rinsed with PBS
639 and dehydrated through a graded ethanol series using microwave-assisted processing (one cycle:
640 1 min on - 1 min off - 1 min on at 100 W). Dehydrated samples were infiltrated with a graded
641 series of HM20 resin (3 minutes per step at 250 W), embedded in gelatin capsules, and
642 polymerized under UV light. Ultrathin ~70 nm sections were prepared using a Leica EM
643 UC6/UC7 ultramicrotome. Sections were blocked with 1% BSA in PBS for 20 minutes, followed
644 by overnight incubation at 4 °C with a primary anti-VPS4A antibody (Cat# 14272-1-AP,
645 Proteintech, IL, USA). After three PBS washes, sections were incubated with an Alexa Fluor 488-
646 conjugated anti-rabbit secondary antibody (Cat# A-11008, Invitrogen, MA, USA). Imaging was
647 performed using a ZEISS LSM 780 Upright Confocal Microscope (ZEISS, Oberkochen,
648 Germany). Calcofluor White binds to chitin and cellulose present in algal cell walls but does not
649 stain *P. bursaria* host cell structures, providing specificity for identifying the algal cell boundary
650 within the host cytoplasm. For cell wall staining, ultrathin sections were stained with Calcofluor
651 White stain (Cat# 18909, Sigma-Aldrich) for 5 minutes and then rinsed with PBS prior to
652 imaging.

653 To obtain quantitative measurements of algal autofluorescence (Cy5 channel) and lipid
654 droplet signals at scale, we employed the ImageXpress® Confocal HT.ai High-Content Imaging
655 System (Molecular Devices, CA, USA), this system is equipped with an automated autofocus
656 function, which selects the optically brightest and sharpest focal plane for each field of view—
657 ensuring consistent imaging quality across hundreds of cells, which enabled high-throughput
658 scanning and analysis of hundreds of *P. bursaria* cells under symbiotic and aposymbiotic
659 conditions.

660

661 **Transmission electron microscopy (TEM) imaging**

662 *P. bursaria* cells were collected and fixed in a mixed aldehyde solution containing 2.5%
663 glutaraldehyde (GA) and 4% paraformaldehyde (PFA) in 100 mM sodium cacodylate buffer (pH
664 7.2). Fixation was performed using a microwave. Samples were irradiated at 500W for 1 min,
665 followed by a 30-s pause, and then an additional 1-min irradiation under vacuum (20 in. Hg). This
666 cycle was repeated eight times. After the final microwave cycle, samples were shaken for 30 min
667 at room temperature, followed by an additional 2 h of shaking before overnight storage at 4 °C.

668 Following fixation, samples were rinsed in 100 mM sodium cacodylate buffer (pH 7.2)
669 under microwave conditions of 150W for 1 min, repeated four times, with no vacuum applied.
670 Post-fixation was performed using 1% osmium tetroxide (OsO_4) in 100 mM sodium cacodylate
671 buffer (pH 7.2). The post-fixation process followed similar microwave conditions: 450W for 1
672 min, followed by a 30-s pause, and another 1-min irradiation under a 20-in. Hg vacuum. This
673 cycle was repeated eight times, with samples shaken at room temperature for 30 min after each
674 cycle, followed by a final 2-h shaking period before overnight storage at 4 °C.

675 After post-fixation, samples were rinsed with distilled water (ddH_2O) under microwave
676 conditions of 150W for 1 min, repeated four times, without a vacuum. En-bloc staining was
677 performed using 2% uranyl acetate (UA). The staining process was carried out under microwave
678 irradiation at 450W for 1 min, followed by a 30-s pause, and another 1-min of irradiation with a
679 vacuum of 20 in. Hg. After staining, samples were rinsed with ddH_2O, with four cycles of
680 microwave irradiation at 150W for 1 min per cycle, without a vacuum. Samples were then
681 dehydrated through a graded ethanol series (10%, 20%, 30%, 40%, 50%, 60%, 70%, 80%, 90%,
682 and 100%). Each ethanol step involved microwave irradiation at 200W for 10 s, followed by a
683 pause of 20 s, and another 10-s irradiation. This process was repeated twice for each ethanol
684 concentration, without a vacuum.

685 Following dehydration, resin infiltration was carried out using spurr's resin without an
686 accelerator. Initially, 5% spurr's resin was applied for 2 days at room temperature. Samples were
687 then infiltrated through a graded resin series (10% to 100%) under a vacuum, with shaking every
688 8 hours. Two changes of 100% spurr's resin without accelerator were applied at 8-h intervals
689 under a vacuum, followed by three changes of 100% spurr's resin with the accelerator under the
690 same conditions. Finally, resin-infiltrated samples were embedded in molds and polymerized in a
691 pre-warmed oven at 70 °C for 24 hours.

692

693 **Statistical Analysis**

694 Statistical tests used in this study are described in the corresponding Methods subsections and
695 figure legends. Unless otherwise noted, P values from enrichment analyses were corrected for
696 multiple comparisons using the Bonferroni correction with a 5% FDR cutoff. Proteins with a
697 missing value in any fraction were excluded from classification analysis. No statistical methods
698 were used to predetermine the sample size. The experiments were not randomized and the
699 investigators were not blinded to allocation during experiments and outcome assessment.
700

701 **References**

702

703 1. M. C. Rivera, R. Jain, J. E. Moore, J. A. Lake, Genomic evidence for two functionally
704 distinct gene classes. *Proc Natl Acad Sci U S A* **95**, 6239-6244 (1998).
705 2. J. Brueckner, W. F. Martin, Bacterial genes outnumber archaeal genes in eukaryotic
706 genomes. *Genome Biol Evol* **12**, 282-292 (2020).
707 3. S. Sudakaran, C. Kost, M. Kaltenpoth, Symbiont acquisition and replacement as a source of
708 ecological innovation. *Trends Microbiol* **25**, 375-390 (2017).
709 4. T. Wein, D. Romero Picazo, F. Blow, C. Woehle, E. Jami, T. B. H. Reusch, W. F. Martin, T.
710 Dagan, Currency, exchange, and inheritance in the evolution of symbiosis. *Trends Microbiol*
711 **27**, 836-849 (2019).
712 5. S. E. Douglas, Plastid evolution: origins, diversity, trends. *Curr Opin Genet Dev* **8**, 655-661
713 (1998).
714 6. J. A. Ochoa de Alda, R. Esteban, M. L. Diago, J. Houmard, The plastid ancestor originated
715 among one of the major cyanobacterial lineages. *Nat Commun* **5**, 4937 (2014).
716 7. I. Zilber-Rosenberg, E. Rosenberg, Role of microorganisms in the evolution of animals and
717 plants: the hologenome theory of evolution. *FEMS Microbiol Rev* **32**, 723-735 (2008).
718 8. M. Ishikawa, I. Yuyama, H. Shimizu, M. Nozawa, K. Ikeo, T. Gojobori, Different
719 endosymbiotic interactions in two Hydra species reflect the evolutionary history of
720 endosymbiosis. *Genome Biol Evol* **8**, 2155-2163 (2016).
721 9. M. Hamada, K. Schroder, J. Bathia, U. Kurn, S. Fraune, M. Khalturina, K. Khalturin, C.
722 Shinzato, N. Satoh, T. C. Bosch, Metabolic co-dependence drives the evolutionarily ancient
723 *Hydra-Chlorella* symbiosis. *Elife* **7**, (2018).
724 10. G. F. Esteban, T. Fenchel, B. J. Finlay, Mixotrophy in ciliates. *Protist* **161**, 621-641 (2010).
725 11. M. Fujishima, *Endosymbionts in Paramecium* M. Fujishima Ed (Microbiolgy Monographs,
726 Springer, 2009), vol. 12.
727 12. Y. Kodama, M. Fujishima, Cycloheximide induces synchronous swelling of perialgal
728 vacuoles enclosing symbiotic *Chlorella vulgaris* and digestion of the algae in the ciliate
729 *Paramecium bursaria*. *Protist* **159**, 483-494 (2008).
730 13. A. Ayala, D. S. Weis, The effect of puromycin and cycloheximide on the infection of algae-
731 free *Paramecium bursaria* by symbiotic Chlorellae. *J Protozool* **34**, 377-381 (1987).
732 14. R. Meier, W. Wiessner, Infection of algae-free *Paramecium bursaria* with symbiotic
733 *Chlorella* sp. Isolated from green paramecia: I. Effect of the incubation period. *Eur J*
734 *Protistol* **24**, 69-74 (1988).
735 15. H. Long, P. Johri, J. F. Gout, J. Ni, Y. Hao, T. Licknack, Y. Wang, J. Pan, B. Jimenez-Marin,
736 M. Lynch, *Paramecium* genetics, genomics, and evolution. *Annu Rev Genet* **57**, 391-410
737 (2023).
738 16. Y. Gao, T. Solberg, R. Wang, Y. Yu, K. A. S. Al-Rasheid, F. Gao, Application of RNA

739 interference and protein localization to investigate housekeeping and developmentally
740 regulated genes in the emerging model protozoan *Paramecium caudatum*. *Commun Biol* **7**,
741 204 (2024).
742 17. B. H. Jenkins, F. Maguire, G. Leonard, J. D. Eaton, S. West, B. E. Housden, D. S. Milner,
743 T. A. Richards, Emergent RNA-RNA interactions can promote stability in a facultative
744 phototrophic endosymbiosis. *Proc Natl Acad Sci U S A* **118**, (2021).
745 18. K. Hauser, W. J. Haynes, C. Kung, H. Plattner, R. Kissmehl, Expression of the green
746 fluorescent protein in *Paramecium tetraurelia*. *Eur J Cell Biol* **79**, 144-149 (2000).
747 19. Y. H. Cheng, C. J. Liu, Y. H. Yu, Y. T. Jhou, M. Fujishima, I. J. Tsai, J. Y. Leu, Genome
748 plasticity in *Paramecium bursaria* revealed by population genomics. *BMC Biol* **18**, 180
749 (2020).
750 20. M. Lynch, P. E. Schavemaker, T. J. Licknack, Y. Hao, A. Pezzano, Evolutionary
751 bioenergetics of ciliates. *J Eukaryot Microbiol* **69**, e12934 (2022).
752 21. M. Fujishima, Y. Kodama, Endosymbionts in paramecium. *Eur J Protistol* **48**, 124-137
753 (2012).
754 22. R. Aebersold, M. Mann, Mass-spectrometric exploration of proteome structure and
755 function. *Nature* **537**, 347-355 (2016).
756 23. A. Mund, A. D. Brunner, M. Mann, Unbiased spatial proteomics with single-cell resolution
757 in tissues. *Mol Cell* **82**, 2335-2349 (2022).
758 24. M. He, J. Wang, X. Fan, X. Liu, W. Shi, N. Huang, F. Zhao, M. Miao, Genetic basis for the
759 establishment of endosymbiosis in *Paramecium*. *Isme J* **13**, 1360-1369 (2019).
760 25. E. C. Su, H. S. Chiu, A. Lo, J. K. Hwang, T. Y. Sung, W. L. Hsu, Protein subcellular
761 localization prediction based on compartment-specific features and structure conservation.
762 *BMC Bioinformatics* **8**, 330 (2007).
763 26. Y. Kodama, M. Fujishima, Endosymbiotic *Chlorella variabilis* reduces mitochondrial
764 number in the ciliate *Paramecium bursaria*. *Sci Rep* **12**, 8216 (2022).
765 27. Y. Kodama, H. Sumita, The ciliate *Paramecium bursaria* allows budding of symbiotic
766 *Chlorella variabilis* cells singly from the digestive vacuole membrane into the cytoplasm
767 during algal reinfection. *Protoplasma* **259**, 117-125 (2022).
768 28. C. Song, K. Murata, T. Suzaki, Intracellular symbiosis of algae with possible involvement
769 of mitochondrial dynamics. *Sci Rep* **7**, 1221 (2017).
770 29. D. N. Itzhak, J. P. Schessner, G. H. H. Borner, Dynamic Organellar Maps for spatial
771 proteomics. *Curr Protoc Cell Biol* **83**, e81 (2019).
772 30. N. M. Moloney, K. Barylyuk, E. Tromer, O. M. Crook, L. M. Breckels, K. S. Lilley, R. F.
773 Waller, P. MacGregor, Mapping diversity in African trypanosomes using high resolution
774 spatial proteomics. *Nat Commun* **14**, 4401 (2023).
775 31. S. J. Karakashian, M. A. Rudzinska, Inhibition of lysosomal fusion with symbiont-
776 containing vacuoles in *Paramecium bursaria*. *Exp Cell Res* **131**, 387-393 (1981).
777 32. F. K. Gu, L. Chen, B. Ni, X. M. Zhang, A comparative study on the electron microscopic
778 enzymo-cytochemistry of *Paramecium bursaria* from light and dark cultures. *Eur J*
779 *Protistol* **38**, 267-278 (2002).
780 33. F. Pedregosa, G. Varoquaux, A. Gramfort, V. Michel, B. Thirion, O. Grisel, M. Blondel, P.
781 Prettenhofer, R. Weiss, V. Dubourg, J. Vanderplas, A. Passos, D. Cournapeau, M. Brucher,
782 M. Perrot, E. Duchesnay, Scikit-learn: machine learning in Python. *J Mach Learn Res* **12**,
783 2825-2830 (2011).
784 34. D. N. Itzhak, S. Tyanova, J. Cox, G. H. Borner, Global, quantitative and dynamic mapping
785 of protein subcellular localization. *Elife* **5**, (2016).
786 35. V. Thumuluri, J. J. Almagro Armenteros, A. R. Johansen, H. Nielsen, O. Winther, DeepLoc
787 2.0: multi-label subcellular localization prediction using protein language models. *Nucleic*
788 *Acids Res* **50**, W228-W234 (2022).

36. D. C. Pease, The structure of trichocysts revealed by the electron microscope. *J Cell Comp Physiol* **29**, 91-94 (1947).
37. H. Plattner, Trichocysts-*Paramecium*'s Projectile-like Secretory Organelles: Reappraisal of their Biogenesis, Composition, Intracellular Transport, and Possible Functions. *J Eukaryot Microbiol* **64**, 106-133 (2017).
38. S. Gurung, D. Perocheau, L. Touramanidou, J. Baruteau, The exosome journey: from biogenesis to uptake and intracellular signalling. *Cell Commun Signal* **19**, 47 (2021).
39. J. Hallgren, K. D. Tsirigos, M. D. Pedersen, J. J. Almagro Armenteros, P. Marcatili, H. Nielsen, A. Krogh, O. Winther, DeepTMHMM predicts alpha and beta transmembrane proteins using deep neural networks. *bioRxiv*, 2022.2004.2008.487609 (2022).
40. N. Jacquier, V. Choudhary, M. Mari, A. Toulmay, F. Reggiori, R. Schneiter, Lipid droplets are functionally connected to the endoplasmic reticulum in *Saccharomyces cerevisiae*. *J Cell Sci* **124**, 2424-2437 (2011).
41. F. Wilfling, H. Wang, J. T. Haas, N. Krahmer, T. J. Gould, A. Uchida, J. X. Cheng, M. Graham, R. Christiano, F. Frohlich, X. Liu, K. K. Buhman, R. A. Coleman, J. Bewersdorf, R. V. Farese, Jr., T. C. Walther, Triacylglycerol synthesis enzymes mediate lipid droplet growth by relocalizing from the ER to lipid droplets. *Dev Cell* **24**, 384-399 (2013).
42. A. R. Thiam, R. V. Farese, Jr., T. C. Walther, The biophysics and cell biology of lipid droplets. *Nat Rev Mol Cell Biol* **14**, 775-786 (2013).
43. N. Kory, R. V. Farese, Jr., T. C. Walther, Targeting fat: Mechanisms of protein localization to lipid droplets. *Trends Cell Biol* **26**, 535-546 (2016).
44. D. T. Haas, D. Weindl, P. Kakimoto, E. M. Trautmann, J. P. Schessner, X. Mao, M. J. Gerl, M. Gerwien, T. D. Muller, C. Klose, X. Cheng, J. Hasenauer, N. Krahmer, C-COMPASS: a user-friendly neural network tool profiles cell compartments at protein and lipid levels. *Nat Methods* **23**, 118-130 (2026).
45. Y. Kodama, M. Fujishima, Timing of perialgal vacuole membrane differentiation from digestive vacuole membrane in infection of symbiotic algae *Chlorella vulgaris* of the ciliate *Paramecium bursaria*. *Protist* **160**, 65-74 (2009).
46. T. C. Walther, R. V. Farese, Jr., Lipid droplets and cellular lipid metabolism. *Annu Rev Biochem* **81**, 687-714 (2012).
47. J. A. Olzmann, P. Carvalho, Dynamics and functions of lipid droplets. *Nat Rev Mol Cell Biol* **20**, 137-155 (2019).
48. J. Morales, G. Ehret, G. Poschmann, T. Reinicke, A. K. Maurya, L. Kroninger, D. Zanini, R. Wolters, D. Kalyanaraman, M. Krakovka, M. Baumers, K. Stuhler, E. C. M. Nowack, Host-symbiont interactions in *Angomonas deane*i include the evolution of a host-derived dynamin ring around the endosymbiont division site. *Curr Biol* **33**, 28-40 e27 (2023).
49. E. C. Nowack, A. R. Grossman, Trafficking of protein into the recently established photosynthetic organelles of *Paulinella chromatophora*. *Proc Natl Acad Sci U S A* **109**, 5340-5345 (2012).
50. K. C. Cook, J. A. Moreno, P. M. Jean Beltran, I. M. Cristea, Peroxisome plasticity at the virus-host interface. *Trends Microbiol* **27**, 906-914 (2019).
51. F. Di Cara, Peroxisomes in host defense. *PLoS Pathog* **16**, e1008636 (2020).
52. P. M. Jean Beltran, K. C. Cook, Y. Hashimoto, C. Galitzine, L. A. Murray, O. Vitek, I. M. Cristea, Infection-induced peroxisome biogenesis is a metabolic strategy for herpesvirus replication. *Cell Host Microbe* **24**, 526-541 e527 (2018).
53. G. Boncompain, C. Muller, V. Meas-Yedid, P. Schmitt-Kopplin, P. B. Lazarow, A. Subtil, The intracellular bacteria *Chlamydia* hijack peroxisomes and utilize their enzymatic capacity to produce bacteria-specific phospholipids. *PLoS One* **9**, e86196 (2014).
54. M. M. Kamal, Y. H. Cheng, L. W. Chu, P. T. Nguyen, C. J. Liu, C. W. Liao, T. Posch, J. Y. Leu, Environment-dependent mutualism-parasitism transitions in the incipient symbiosis

839 between *Tetrahymena utriculariae* and *Micractinium tetrahymenae*. *Isme J* **19**, (2025).
840 55. C. Londos, C. Sztalryd, J. T. Tansey, A. R. Kimmel, Role of PAT proteins in lipid
841 metabolism. *Biochimie* **87**, 45-49 (2005).
842 56. M. Rogne, K. Tasken, Compartmentalization of cAMP signaling in adipogenesis,
843 lipogenesis, and lipolysis. *Horm Metab Res* **46**, 833-840 (2014).
844 57. C. L. Yen, S. J. Stone, S. Koliwad, C. Harris, R. V. Farese, Jr., Thematic review series:
845 glycerolipids. DGAT enzymes and triacylglycerol biosynthesis. *J Lipid Res* **49**, 2283-2301
846 (2008).
847 58. S.-E. Peng, Y.-B. Wang, L.-H. Wang, W.-N. U. Chen, C.-Y. Lu, L.-S. Fang, C.-S. Chen,
848 Proteomic analysis of symbiosome membranes in Cnidaria–dinoflagellate endosymbiosis.
849 *Proteomics* **10**, 1002-1016 (2010).
850 59. H. Stenmark, Rab GTPases as coordinators of vesicle traffic. *Nature Reviews Molecular*
851 *Cell Biology* **10**, 513-525 (2009).
852 60. M. Babst, B. Wendland, E. J. Estepa, S. D. Emr, The Vps4p AAA ATPase regulates
853 membrane association of a Vps protein complex required for normal endosome function.
854 *The EMBO Journal* **17**, 2982-2993 (1998).
855 61. J. H. Hurley, P. I. Hanson, Membrane budding and scission by the ESCRT machinery: it's
856 all in the neck. *Nature Reviews Molecular Cell Biology* **11**, 556-566 (2010).
857 62. N. Krahmer, M. Hilger, N. Kory, F. Wilfling, G. Stoehr, M. Mann, R. V. Farese, Jr., T. C.
858 Walther, Protein correlation profiles identify lipid droplet proteins with high confidence.
859 *Mol Cell Proteomics* **12**, 1115-1126 (2013).
860 63. G. H. H. Borner, Organellar maps through proteomic profiling - a conceptual guide. *Mol*
861 *Cell Proteomics* **19**, 1076-1087 (2020).
862 64. C. J. Crossland, D. J. Barnes, M. A. Borowitzka, Diurnal lipid and mucus production in the
863 staghorn coral *Acropora acuminata*. *Mar Biol* **60**, 81-90 (1980).
864 65. S. E. Peng, W. N. Chen, H. K. Chen, C. Y. Lu, A. B. Mayfield, L. S. Fang, C. S. Chen, Lipid
865 bodies in coral-dinoflagellate endosymbiosis: proteomic and ultrastructural studies.
866 *Proteomics* **11**, 3540-3555 (2011).
867 66. H. K. Chen, L. H. Wang, W. U. Chen, A. B. Mayfield, O. Levy, C. S. Lin, C. S. Chen, Coral
868 lipid bodies as the relay center interconnecting diel-dependent lipidomic changes in
869 different cellular compartments. *Sci Rep* **7**, 3244 (2017).
870 67. A. Catacora-Grundy, F. Chevalier, D. Yee, C. LeKieffre, N. L. Schieber, Y. Schwab, B.
871 Gallet, P. H. Jouneau, G. Curien, J. Decelle, Sweet and fatty symbionts: photosynthetic
872 productivity and carbon storage boosted in microalgae within a host. *bioRxiv*,
873 2023.2012.2022.572971 (2023).
874 68. P. T. Dong, J. Tian, K. J. Kobayashi-Kirschvink, L. Cen, J. S. McLean, B. Bor, W. Shi, X.
875 He, Episymbiotic *Saccharibacteria* induce intracellular lipid droplet production in their host
876 bacteria. *Isme J* **18**, (2024).
877 69. P. Roingeard, R. C. Melo, Lipid droplet hijacking by intracellular pathogens. *Cell Microbiol*
878 **19**, (2017).
879 70. L. A. Mota, J. Roberto Neto, V. G. Monteiro, C. S. Lobato, M. A. Oliveira, M. Cunha, H.
880 D'Avila, S. H. Seabra, P. T. Bozza, R. A. DaMatta, Culture of mouse peritoneal macrophages
881 with mouse serum induces lipid bodies that associate with the parasitophorous vacuole and
882 decrease their microbicidal capacity against *Toxoplasma gondii*. *Mem Inst Oswaldo Cruz*
883 **109**, 767-774 (2014).
884 71. S. J. Nolan, J. D. Romano, I. Coppens, Host lipid droplets: An important source of lipids
885 salvaged by the intracellular parasite *Toxoplasma gondii*. *PLoS Pathog* **13**, e1006362
886 (2017).
887 72. H. Hosoya, K. Kimura, S. Matsuda, M. Kitaura, T. Takahashi, T. Kosaka, Symbiotic algae-
888 free strains of the green paramecium *Paramecium bursaria* produced by herbicide paraquat.

Zool Sci **12**, 807-810 (1995).
73. C. W. Chen, C. F. Tsai, M. H. Lin, S. Y. Lin, C. C. Hsu, Suspension trapping-based sample preparation workflow for in-depth plant phosphoproteomics. *Anal Chem* **95**, 12232-12239 (2023).
74. T. J. Licknack, "A spatial proteome of *Paramecium tetraurelia*", thesis, Arizona State University, ASU Library (2022).
75. D. M. Emms, S. Kelly, OrthoFinder: solving fundamental biases in whole genome comparisons dramatically improves orthogroup inference accuracy. *Genome Biol* **16**, 157 (2015).
76. A. Geladaki, N. Kocevar Britovsek, L. M. Breckels, T. S. Smith, O. L. Vennard, C. M. Mulvey, O. M. Crook, L. Gatto, K. S. Lilley, Combining LOPIT with differential ultracentrifugation for high-resolution spatial proteomics. *Nat Commun* **10**, 331 (2019).
77. J. P. Schessner, V. Albrecht, A. K. Davies, P. Sinitcyn, G. H. H. Borner, Deep and fast label-free Dynamic Organellar Mapping. *Nat Commun* **14**, 5252 (2023).
78. M. Blum, H. Y. Chang, S. Chuguransky, T. Grego, S. Kandasaamy, A. Mitchell, G. Nuka, T. Paysan-Lafosse, M. Qureshi, S. Raj, L. Richardson, G. A. Salazar, L. Williams, P. Bork, A. Bridge, J. Gough, D. H. Haft, I. Letunic, A. Marchler-Bauer, H. Mi, D. A. Natale, M. Necci, C. A. Orengo, A. P. Pandurangan, C. Rivoire, C. J. A. Sigrist, I. Sillitoe, N. Thanki, P. D. Thomas, S. C. E. Tosatto, C. H. Wu, A. Bateman, R. D. Finn, The InterPro protein families and domains database: 20 years on. *Nucleic Acids Res* **49**, D344-D354 (2021).
79. D. Szklarczyk, R. Kirsch, M. Koutrouli, K. Nastou, F. Mehryary, R. Hachilif, A. L. Gable, T. Fang, N. T. Doncheva, S. Pyysalo, P. Bork, L. J. Jensen, C. von Mering, The STRING database in 2023: protein-protein association networks and functional enrichment analyses for any sequenced genome of interest. *Nucleic Acids Res* **51**, D638-D646 (2023).
80. V. Gligorijevic, P. D. Renfrew, T. Kosciolek, J. K. Leman, D. Berenberg, T. Vatanen, C. Chandler, B. C. Taylor, I. M. Fisk, H. Vlamakis, R. J. Xavier, R. Knight, K. Cho, R. Bonneau, Structure-based protein function prediction using graph convolutional networks. *Nat Commun* **12**, 3168 (2021).
81. P. Toronen, A. Medlar, L. Holm, PANNZER2: a rapid functional annotation web server. *Nucleic Acids Res* **46**, W84-W88 (2018).
82. F. Klingelhuber, S. Frendo-Cumbo, M. Omar-Hmeadi, L. Massier, P. Kakimoto, A. J. Taylor, M. Couchet, S. Ribicic, M. Wabitsch, A. C. Messias, A. Iuso, T. D. Muller, M. Ryden, N. Mejhert, N. Krahmer, A spatiotemporal proteomic map of human adipogenesis. *Nat Metab* **6**, 861-879 (2024).

Acknowledgments

We thank members of the Leu lab for helpful discussion and comments on the manuscript. We also thank John O'Brien for manuscript editing, the IMB Imaging Core for imaging experiments, and the IPMB Proteomics Core for proteomics experiments. We thank Professor Toshinobu Suzaki (Kobe University, Japan) for helping us set the *Chlorogonium capillatum* feeding axenic method for *P. bursaria* cell culture. We would like to dedicate this paper to the memory of Dr. Meng-Chao Yao (1949-2025), a great mentor and excellent ciliate biologist, who inspires us to work on ciliates

Funding: This work was supported by Academia Sinica of Taiwan (grant no. AS-IA-110-L01 and AS-GCS-113-L03).

This work was supported by the National Science and Technology Council of Taiwan (NSTC 113-2326-B-001-002).
MMK was supported by an NSTC postdoctoral fellowship (NSTC 113-2811-B-001-065).

Author contributions:

Conceptualization: MMK, JYL
Methodology: YJC, MMK, JYL
Investigation: YJC, MMK, CCH
Formal analysis: YJC, MMK, CCH
Data curation: YJC, MMK
Software: YJC, MMK
Visualization: YJC, MMK
Resources: JYL
Supervision: JYL
Writing-original draft: YJC, MMK, JYL
Writing-review & editing: YJC, MMK, CCH, JYL

Competing interests: The authors declare that they have no competing interests.

Data and materials availability

The mass spectrometry proteomics data have been deposited in the ProteomeXchange Consortium under accession numbers PXD055842 and PXD055875. Additional data generated or analyzed in this study are provided as Data files and Source Data files with this article.

957 **Figures**

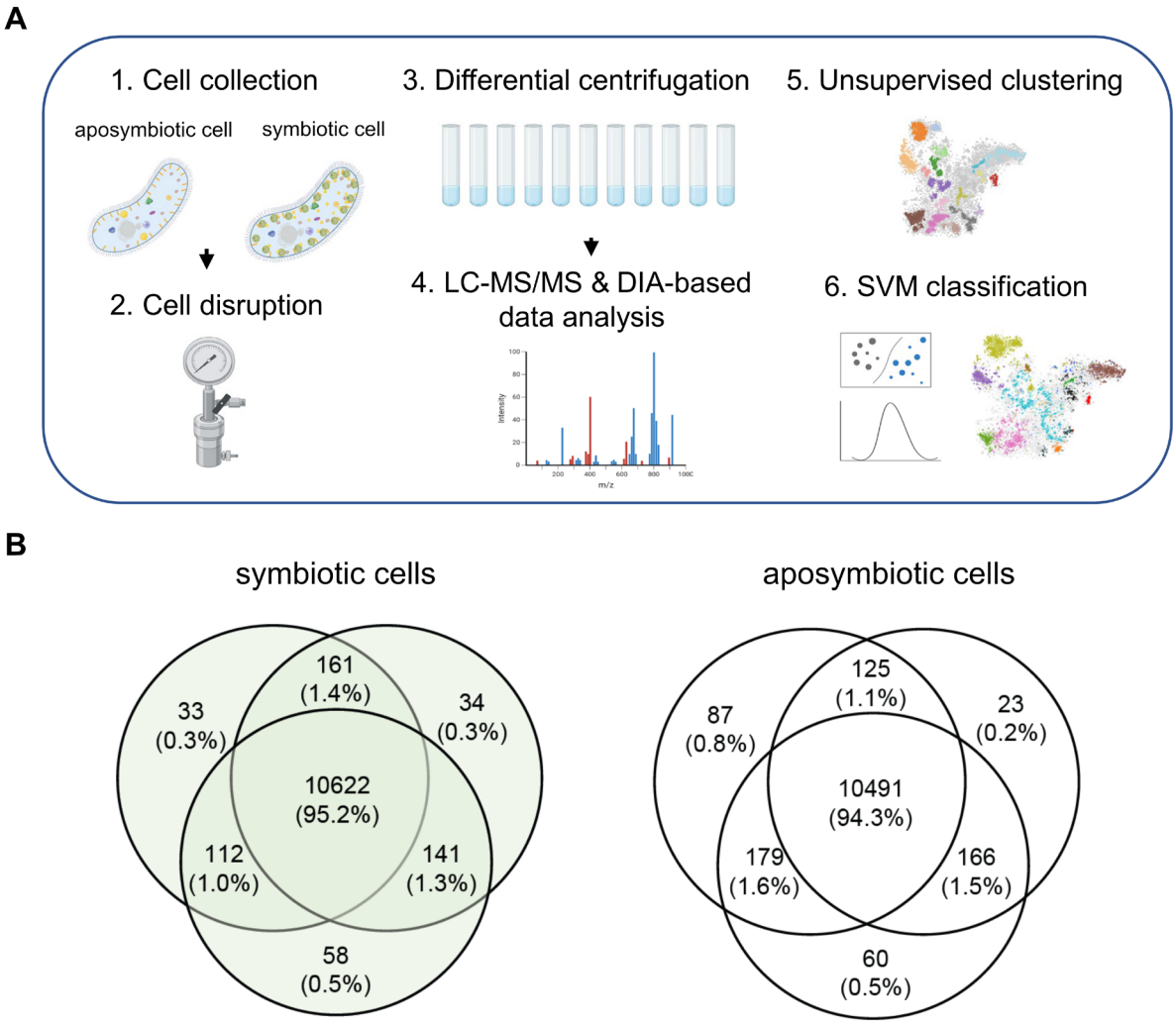

958

959 **Fig. 1. Application of differential centrifugation to separate subcellular compartments of *P.***
960 ***bursaria* cells.**

961 **(A)** Workflow of *P. bursaria* subcellular localization mapping by differential centrifugation. *P.*
962 *bursaria* cells with (symbiotic cell) or without (aposymbiotic cell) endosymbionts were lysed by
963 nitrogen cavitation and the subcellular compartments were separated by differential
964 centrifugation. Subcellular compartment fractions were collected and analyzed by DIA-LC/MS.
965 Protein profiles were generated, subjected to unsupervised clustering, and used to predict protein
966 localizations using SVM machine learning. **(B)** Venn diagrams showing the number of proteins
967 identified in three replicate experiments. The final datasets contained 10622 proteins for
968 symbiotic cells and 10491 proteins for aposymbiotic cells.

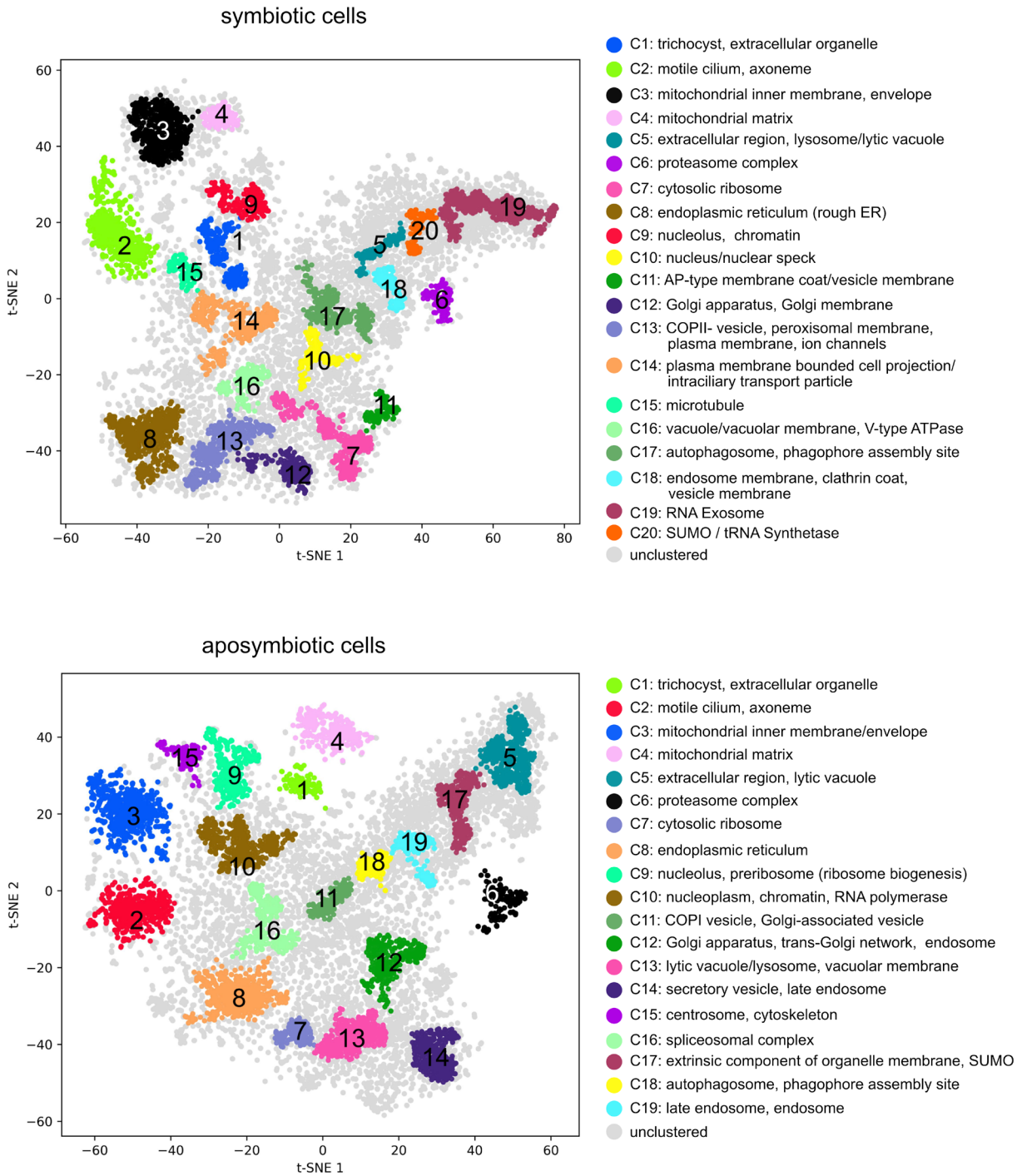

Fig. 2. Unsupervised clusters demonstrate a resolution of distinct subcellular functional compartments in *P. bursaria*.

HDBSCAN clusters are highlighted on t-SNE projections for **(A)** symbiotic *P. bursaria* cells and **(B)** aposymbiotic *P. bursaria* cells. Each point represents a protein. Most significantly over-represented GOCC terms in each cluster are shown in the right panel, indicating that most clusters have distinct biological functions. In our enrichment test, only terms with an enrichment score greater than 2 and an adjusted *P* value less than 0.05 were selected (see also data file S3C,D).

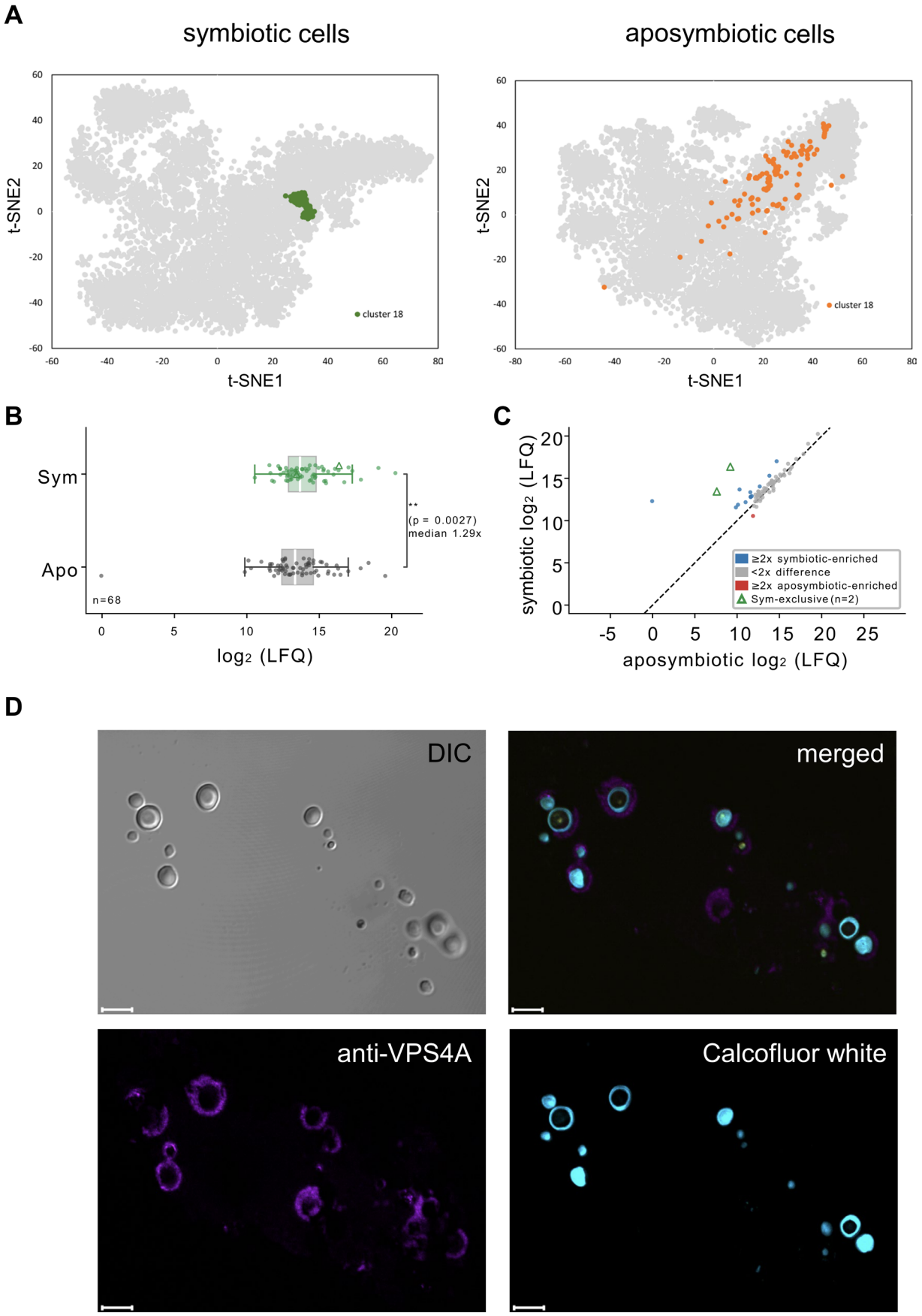
A
symbiotic cells
aposymbiotic cells
t-SNE2
t-SNE1
cluster 18
B
Sym
Apo
n=68
**
(p = 0.0027)
median 1.29x
log2 (LFQ)
C
symbiotic log2 (LFQ)
aposymbiotic log2 (LFQ)
≥2x symbiotic-enriched
<2x difference
≥2x aposymbiotic-enriched
Sym-exclusive (n=2)
D
DIC
merged
anti-VPS4A
Calcofluor white

977

978

979 **Fig. 3. Cluster 18 of the HDBSCAN clusters in symbiotic cells is probably formed by the**
980 **proteins of perialgal vacuoles.**
981 **(A)** The cluster 18 proteins in symbiotic cells are not clustered in aposymbiotic cells. **(B)** The
982 proteins of cluster 18 in symbiotic cells (Sym) have higher abundance than those in aposymbiotic
983 cells (Apo). Protein abundance data were obtained from total lysate proteomes (data file S2). **,
984 *P* value < 0.01, Paired-Sample t-test, n = 68 protein groups. Median fold change, 1.29×. **(C)** Per-
985 protein scatter plot showing the abundance of each cluster 18 protein in symbiotic versus
986 aposymbiotic cells. **(D)** Confocal microscopic images show that VPS4A surrounds the symbiotic
987 algal cell wall. Images represent ultrathin (~70 nm) resin sections, providing a cross-sectional
988 view of the perialgal region. Calcofluor White stains the algal cell wall as a spatial reference for
989 perialgal localization. See fig. S3 for whole-cell views comparing VPS4A localization in
990 symbiotic and aposymbiotic cells, including specificity controls with food algae. Scale bar, 5 μm.

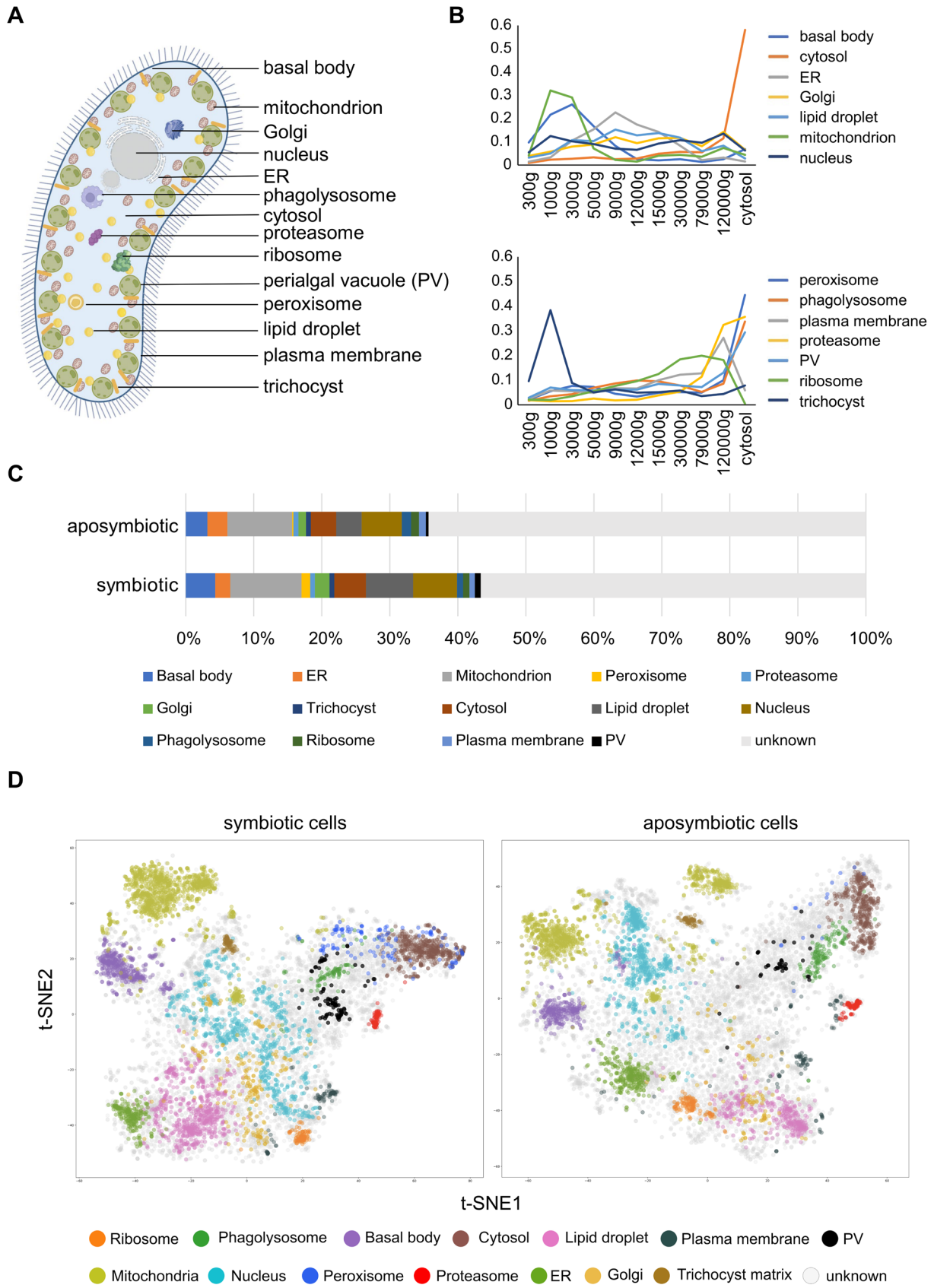

991 **Fig. 4. Subcellular localization maps of symbiotic and aposymbiotic *P. bursaria* cells.**

992 **(A)** Schematic representation of 14 subcellular compartments in *P. bursaria* cells. **(B)** The
993 distribution profiles of marker proteins. All the marker proteins of the same subcellular
994 compartment were averaged and shown. Distribution profiles of individual marker proteins are
995 shown in fig. S4. Since there were 14 subcellular compartments, we split the distribution profiles
996 into two figures to improve clarity. **(C)** Proportions of identified proteins in different subcellular
997 compartments. Protein localization was assigned using SVM-based machine learning. Only
998 protein assignments with medium or higher confidence are shown. Proteins that could not be
999 assigned to a specific compartment were classified into the "unknown" group. **(D)** t-SNE
1000 projections of the proteins assigned to different subcellular compartments in symbiotic *P.*
1001 *bursaria* cells and aposymbiotic *P. bursaria* cells. Each point represents a protein and proteins are
1002 colored according to their subcellular localization.
1003

1004

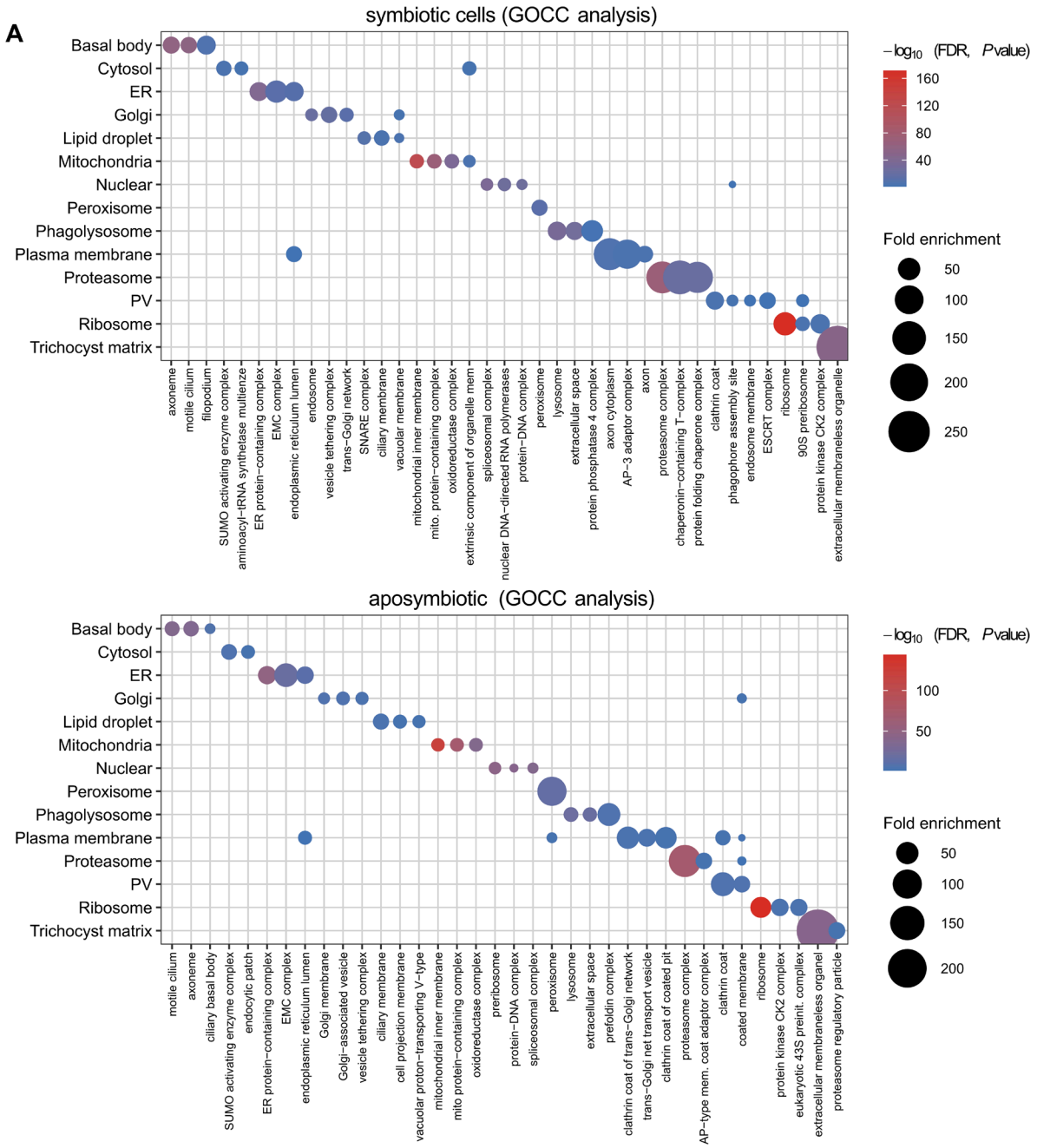
A
symbiotic cells (GOCC analysis)
Basal body
Cytosol
ER
Golgi
Lipid droplet
Mitochondria
Nuclear
Peroxisome
Phagolysosome
Plasma membrane
Proteasome
PV
Ribosome
Trichocyst matrix
axoneme
motile cilium
filopodium
SUMO activating enzyme complex
aminoacyl−tRNA synthetase multienze
ER protein−containing complex
EMC complex
endoplasmic reticulum lumen
endosome
vesicle tethering complex
trans−Golgi network
SNARE complex
ciliary membrane
vacuolar membrane
mitochondrial inner membrane
mito. protein−containing complex
oxidoreductase complex
extrinsic component of organelle mem
spliceosomal complex
nuclear DNA−directed RNA polymerases
protein−DNA complex
peroxisome
lysosome
extracellular space
protein phosphatase 4 complex
axon cytoplasm
AP−3 adaptor complex
axon
proteasome complex
chaperonin−containing T−complex
protein folding chaperone complex
clathrin coat
phagophore assembly site
endosome membrane
ESCRT complex
ribosome
90S preribosome
protein kinase CK2 complex
extracellular membraneless organelle
−log10 (FDR, Pvalue)
160
120
80
40
Fold enrichment
50
100
150
200
250
aposymbiotic (GOCC analysis)
Basal body
Cytosol
ER
Golgi
Lipid droplet
Mitochondria
Nuclear
Peroxisome
Phagolysosome
Plasma membrane
Proteasome
PV
Ribosome
Trichocyst matrix
motile cilium
axoneme
ciliary basal body
SUMO activating enzyme complex
endocytic patch
ER protein−containing complex
EMC complex
endoplasmic reticulum lumen
Golgi membrane
Golgi−associated vesicle
vesicle tethering complex
ciliary membrane
cell projection membrane
vacuolar proton−transporting V−type
mitochondrial inner membrane
mito protein−containing complex
oxidoreductase complex
preribosome
protein−DNA complex
spliceosomal complex
peroxisome
lysosome
extracellular space
prefoldin complex
clathrin coat of trans−Golgi network
trans−Golgi net transport vesicle
clathrin coat of coated pit
proteasome complex
AP−type mem. coat adaptor complex
clathrin coat
coated membrane
ribosome
protein kinase CK2 complex
eukaryotic 43S preinit. complex
extracellular membraneless organel
proteasome regulatory particle
−log10 (FDR, Pvalue)
100
50
Fold enrichment
50
100
150
200

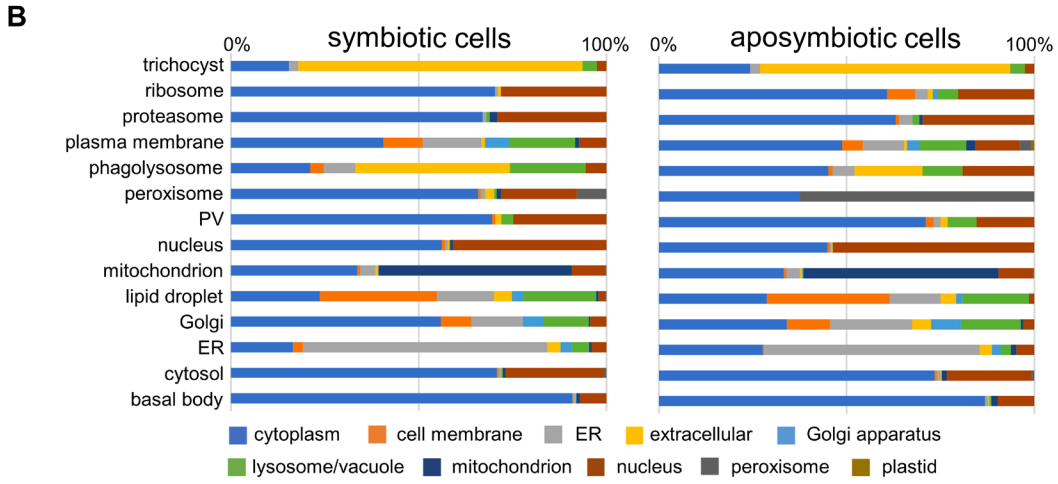
B
symbiotic cells
aposymbiotic cells
0%
100%
trichocyst
ribosome
proteasome
plasma membrane
phagolysosome
peroxisome
PV
nucleus
mitochondrion
lipid droplet
Golgi
ER
cytosol
basal body
cytoplasm
cell membrane
ER
extracellular
Golgi apparatus
lysosome/vacuole
mitochondrion
nucleus
peroxisome
plastid

1005 **Fig. 5. Comparative analysis of spatial proteomes.**

1006 **(A)** Dot plots of the GOCC term enrichment analysis results for symbiotic (top) and aposymbiotic
1007 (bottom) cells. SVM-classified proteins were subjected to GOCC analysis. The Y-axis indicates
1008 the subcellular compartments and the X-axis indicates the enriched GOCC terms. Color is scaled
1009 by $-\log_{10}$(FDR-adjusted P value) and dot size represents fold enrichment. Aposymbiotic cells lack
1010 a true PV; proteins assigned to this compartment by SVM likely represent co-fractionating
1011 endocytic membrane proteins. **(B)** Comparison between the results predicted by the pre-trained
1012 protein language model, DeepLoc 2.0, and our subcellular localization maps. Color coding
1013 represents different predicted subcellular localizations, as determined by DeepLoc 2.0.

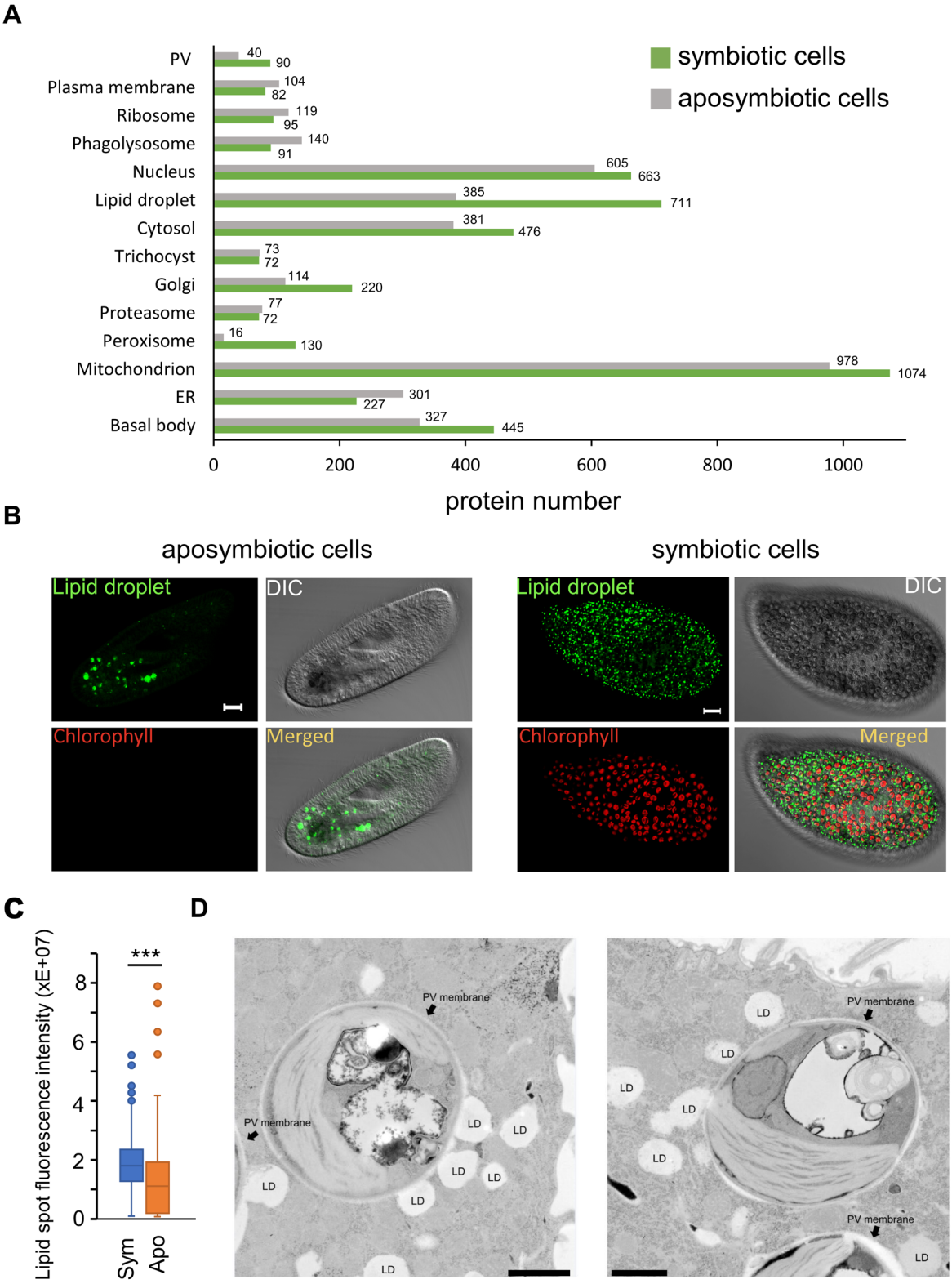

Fig. 6. The morphology and localization of lipid droplets are altered in symbiotic cells. **(A)** Numbers of identified proteins that were assigned to different subcellular compartments in symbiotic and aposymbiotic cells. Total protein numbers are indicated next to each bar. **(B)** Lipid

1018 droplets in aposymbiotic and symbiotic *P. bursaria* cells. Lipid droplets were stained using
1019 LipidSpot (upper panel). **(C)** The LipidSpot fluorescence signal of lipid droplets in symbiotic
1020 cells is significantly higher than that of aposymbiotic cells (lower panel). The Cy5 channel was
1021 used to detect the chlorophyll of endosymbiotic algal cells. Scale bar, 5 μm. ***, P value < 0.001,
1022 Mann-Whitney U test, n ≥ 186 cells. **(D)** Many lipid droplets are attached to the perialgal vacuole
1023 (PV) membrane of the endosymbionts, as revealed by TEM imaging. The arrow indicates the PV
1024 membrane surrounding individual algal cells. Scale bar, 1 μm; LD, lipid droplet.
1025

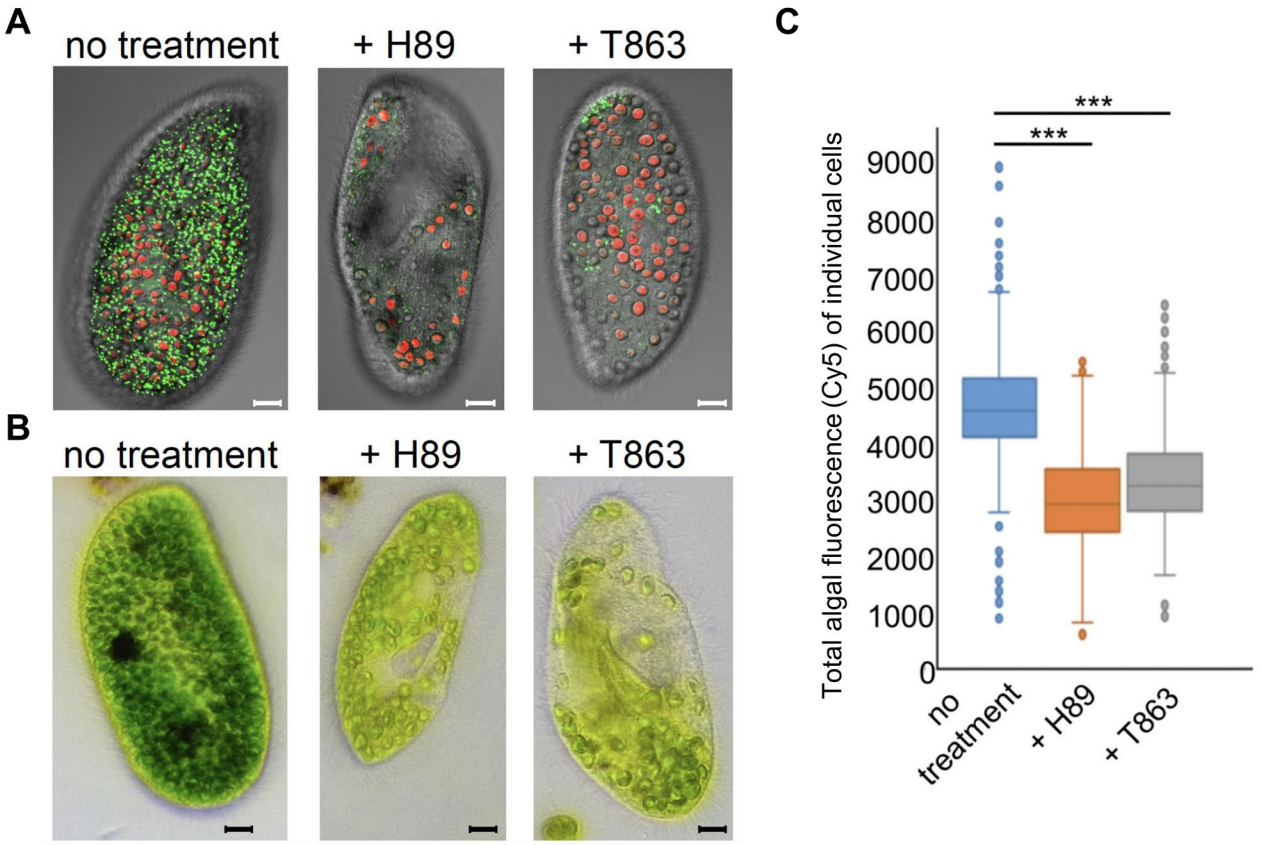

1026

1027 **Fig. 7. Inhibition of lipid metabolism in symbiotic *P. bursaria* cells reduces the**
1028 **endosymbiont number.**

1029 **(A)** Treating symbiotic *P. bursaria* cells with mild doses of lipid metabolism inhibitors H89
1030 (1 μM) or T863 (10 μM) reduces the number of lipid droplets. Lipid droplets (in green) were
1031 stained using LipidSpot. **(B)** H89 or T863 treatment results in a reduced number of endosymbiotic
1032 algae in *P. bursaria* cells. Scale bar, 10 μm. **(C)** Total algal fluorescence (Cy5) of individual cells
1033 is significantly reduced after two weeks of treatment. ***, P value < 0.001, Mann-Whitney U test,
1034 n ≥ 373 *P. bursaria* cells.